Identifying and modeling motion primitives for the hydromedusae *Sarsia tubulosa* and *Aequorea victoria*

2015 Bioinspir. Biomim. 10 066001

(http://iopscience.iop.org/1748-3190/10/6/066001)

Bioinspiration & Biomimetics

RECEIVED
31 March 2015

REVISED
5 August 2015

ACCEPTED FOR PUBLICATION
18 August 2015

PUBLISHED
23 October 2015

Identifying and modeling motion primitives for the hydromedusae *Sarsia tubulosa* and *Aequorea victoria*

Isaac Sledge[1,3], **Michael Krieg**[2,3], **Doug Lipinski**[4] **and Kamran Mohseni**[1,2,3]

[1] Department of Electrical and Computer Engineering, University of Florida, USA
[2] Department of Mechanical and Aerospace Engineering, University of Florida, USA
[3] Institute for Networked Autonomous Systems, University of Florida, USA
[4] Department of Mechanical and Aerospace Engineering, University of Florida, USA

E-mail: mohseni@ufl.edu

Keywords: motion primitive, motion segmentation, dynamics modeling

Abstract

The movements of organisms can be thought of as aggregations of motion primitives: motion segments containing one or more significant actions. Here, we present a means to identify and characterize motion primitives from recorded movement data. We address these problems by assuming that the motion sequences can be characterized as a series of dynamical-system-based pattern generators. By adopting a nonparametric, Bayesian formalism for learning and simplifying these pattern generators, we arrive at a purely data-driven model to automatically identify breakpoints in the movement sequences. We apply this model to swimming sequences from two hydromedusa. The first hydromedusa is the prolate *Sarsia tubulosa*, for which we obtain five motion primitives that correspond to bell cavity pressurization, jet formation, jetting, cavity fluid refill, and coasting. The second hydromedusa is the oblate *Aequorea victoria*, for which we obtain five motion primitives that correspond to bell compression, vortex separation, cavity fluid refill, vortex formation, and coasting. Our experimental results indicate that the breakpoints between primitives are correlated with transitions in the bell geometry, vortex formation and shedding, and changes in derived dynamical quantities. These dynamics quantities include terms like pressure, power, drag, and thrust. Such findings suggest that dynamics information is inherently present in the observed motions.

1. Introduction

Cnidarian medusae are marine invertebrates with a unique body structure. Compared to other aquatic organisms with more complex swimming appendages, medusae have a relatively simple structure consisting of an axisymmetric, umbrella-shaped bell. The bell is the primary swimming appendage and is able to contract by a circular band of muscle fibers. Periodic bell contractions and extensions interact with the surrounding fluid and deliver momentum into the wake to generate locomotive forces.

For medusae with a prolate body (bell height greater than diameter), jetting-based propulsion is their main swimming mechanism. Thrust arises from the forceful expulsion of water from a cavity through the velar aperture. Since there are no muscles to oppose those that expel water, the surrounding fluid is drawn back into the bell by the release of elastic strain energy stored in the bell during contraction. This is similar to a process observed in cephalopods [1]. In short, discontinuous, unsteady motion is produced by a contraction phase during which water is ejected and positive thrust is produced. This is followed by a motionless stage in which either negative or negligible thrust is generated [2]. The temporal nature of the unsteadiness is variable [3, 4], since medusae maneuver in bouts of swimming cycles interspersed with periods of inactivity.

For many years, jetting-based propulsion [5, 6] was viewed as the only swimming mechanism for medusae, and the model proposed in [7, 8] has been applied to a broad range of species to describe their behavior. However, more recent analyses have revealed that such a model is not relevant for all medusae. Colin and Costello [9] found that the work of

Daniel [7, 8] can only explain the acceleration patterns of prolate medusae, not oblate medusae (bell height less than diameter). From their observations and multiple follow-up studies [2, 10], it was determined that oblate medusae swim according to a jet-paddling, or rowing, mode of propulsion [11]. Under this regime, jet-paddling generates a propulsive vortex during the contraction phase. During the relaxation phase, the bell causes the formation of a second vortex with opposite rotation relative to the propulsive vortex. These two vortex rings interact and create large induced velocities away from the hydromedusae in the wake [10].

Despite the differences in swim mechanics, all hydromedusae have a common organization for neuromuscular control [12, 13]. The control framework consists of an electrically coupled network of large neurons found in the bell. These neurons act as a distributed swim pacemaker system, or central pattern generator, for swim contractions. Superimposed on this network are species-specific neuronal and muscular organizations that allow unique behavioral responses for each species.

Due to the utility of these underlying pattern generators for modulating medusae swimming behaviors, we are interested in modeling their motion responses for bio-inspired locomotion and control. That is, we would like a means to describe and transfer many of the witnessed maneuvers. In doing so, it should be possible to quickly and efficiently plan paths using the extracted motions for certain biologically imitative platforms [14]. Understanding the environmental effects of these maneuvers should also help advance actuation schemes [15, 16]. Coupled with this desire is that of improving upon these maneuvers and removing unnecessary elements from them.

To facilitate this motion modeling, it is helpful to have a base characterization of the motions. We hence pursue the identification of motion primitives from recorded observations. This identification is equivalent to temporal motion segmentation. That is, we look for breakpoints where there are either gradual or abrupt changes in the medusae kinematics. Such time instances should correspond to changes in actuation regimes. We simultaneously model the motions as dynamical systems so that swappable, pattern-generator-based controllers can be created. The use of these controllers for driving soft-body platforms will be the subject of our future endeavors.

The motion primitives that we identify are subsets of hydromedusae movement sequences that contain one or more variable-duration actions. For example, a single cycle of a rhythmic propulsion cycle or even a fraction of the cycle could be taken as a motion primitive. At the other extreme, in the case of a forward propulsion and turning action, there would be two major motion templates. One primitive would correspond to the body kinematics up to the turning point and the other to the motions that occur after the turn. Depending upon the needs of the application, these two primitives could be further subdivided.

Although motion primitives can be manually identified, it is advantageous to automate their extraction. This is because it permits the quick analysis of multiple motions and hence should allow us to impart platforms with a wide range of capabilities.

Any motion sequence can be segmented arbitrarily. However, use of the motion subsequences as the foundation for controllers will require that the segmentation breakpoints correspond with meaningful changes in either the hydromedusa's actions or the hydromedusa's influence on the environment. We therefore propose a hybrid motion characterization and segmentation scheme that is based upon learning low-dimensional, stochastic dynamical systems. Under this scheme we concurrently uncover reduced spaces for the movement sequences and characterize the motion dynamics in this simpler space. By simplifying the dynamics, we can construct efficient controllers. Due to the way that we perform this reduction, it becomes easy to detect temporal breakpoints and hence segment the motions. We accomplish this through a generative Bayesian model (see section 2.1 for the overview and section 2.2 for the mathematical details).

To assess our approach, we consider the modeling and segmentation of propulsive motions from the *Sarsia tubulosa*, a jetting-based hydromedusa, and the *Aequorea victoria*, a paddling-based jellyfish. Our experimental results show that the breakpoints occur during major changes in the body kinematics (see sections 3.2.1 and 3.3.1 for an overview of the primitives). Additionally, a comparison against multiple dynamics quantities reveals that the breakpoints are correlated with inflections in terms like thrust, drag, power output, and flow rate (see sections 3.2.2 and 3.3.2 for the dynamics results and discussion). This clear separation of motion dynamics leads us to believe that each primitive is associated with a separate actuation scheme. Therefore, it is plausible that the motion primitives we identify could be swapped in and out to achieve efficient control of soft-body platforms As well, the findings suggest that the bell motions, which are simple to detect and process, inherently encode a great deal of dynamics information.

Before continuing, it is important to note that we are not the first to consider motion primitives: over the years, a variety of motion primitive research has conducted. A majority of these efforts are focused on demonstrating that motion primitives can reduce the computational burdens associated with both low- and high-level robotic control problems [17–25]. In comparison, the automated extraction of motion primitives from movement sequences has received limited attention. This is largely because much of the existing work has focused on platforms with few degrees of freedom, for which motion primitives can be quickly and manually specified by investigators.

As the number of degrees of freedom in a platform increases, however, the problem of defining motion primitives becomes more complicated. By automatically specifying motion primitives from movement sequences, we will save investigators substantial time when defining primitives for such platforms It will also permit bio-inspired platforms to mimic the locomotive behaviors present in the movement sequences. The segmentation scheme developed in this paper therefore represents a much-needed contribution.

2. Motion dynamics learning and segmentation

2.1. Motion processing overview

For our motion modeling and segmentation, we assume that we have sequences of bell kinematics data. We seek to describe this, potentially multi-modal, data by a series of low-dimensional dynamical systems. These low-dimensional systems focus on neighborhoods of the phase space and should evolve in the same manner as the potentially unknown, high-dimensional systems that generated the data. That is, we split the domain into multiple regions according to the local complexity of the phase space. Each region is overseen by a computationally tractable, low-dimensional dynamical system that offers an opinion about the progression of the high-dimensional behaviors. Note the construction of these low-dimensional systems does not require either data pre-processing or any physical insight about the motions.

For our framework, we would like the low-dimensional dynamical systems to function as motion primitives. Where these systems are defined in the phase space should correspond to breakpoints, or meaningful changes, in the motion. These breakpoints match well with the observed dynamics, as we will show in our experiments.

The type of stochastic differential equations used in the model influences how effectively it can characterize kinematics. We have opted to use a superposition of Lévy-driven [26, 27] Gauss–Markov processes [28] with non-Gaussian marginal distributions. Gauss–Markov processes are host to a number of excellent properties [29, 30]. For example, they can be viewed as continuous analogues of first-order autoregressive processes [31]. This property suggests that Gauss–Markov processes should be well suited to modeling motions over short time scales.

If the Gauss–Markov processes are to be of practical use, investigators must have some insights into the structure of the dynamics. As well, investigators would need to know the number of phase-space regions needed to construct a decent approximation. Estimates for the number of motion primitives would therefore need to be supplied. Both of these consequences are counterproductive to our ambitions. This is because we seek an approach for motion modeling that relies on little to no human supervision. To avoid explicitly specifying this information, we adopt a nonparametric model assumption [32]. We assume that a characterization of the motion primitive kinematics may require an infinite superposition of both latent processes and Gauss–Markov processes. In most cases, however, only a finite number of processes will be necessary. A prudent selection of prior distributions will permit our inference scheme to automatically discern the number of Gauss–Markov processes and motion primitives present in the data.

2.2. Bayesian model specification

In what follows, we describe a probabilistic, continuous-time model that relates sequences of motion observations with a number of low-dimensional dynamics systems. For generality, we assume that the discrete-time observations $x_k^m(t) \in \mathbb{R}^d$ may come from $m = 1, \ldots, M$ datasets each potentially having $k = 1, \ldots, K$ modalities. The proposed model consists of $p = 1, \ldots, P$ low-dimensional latent processes $y_k^m(t; p) \in \mathbb{R}^q$, $q < d$, which evolve independently of each other and are described by a set of stochastic, parameterized partial differential equations [33]. These stochastic differential equations impose a prior distribution on the space of latent processes. They encode any prior knowledge about how a hydromedusa's body may change in shape.

Some simplifying suppositions need to be made about these latent processes so that our model is tractable. The first supposition is stationarity of the reduced dynamics evolution. That is, unless there is information suggesting to the contrary, we do not want to impose a bias on how the latent dynamics processes change over time. Note that a combination of the latent processes will be capable of modeling nonstationary movement dynamics.

Additionally, we would like the correlation between two instances of the latent process to decay monotonically as time between them grows. Eventually, we want the correlation to approach total independence as the time between instances becomes unbounded. This implies that the dynamics at one time instant should not strongly influence the dynamics in the distant future. We therefore cannot make use of any models that do not account for the temporal evolution of the latent processes and assume that the latent states are not time-dependent.

Lastly, we enforce continuity with an analytically available transition density. Such a constraint allows for statistical model inference to be carried out even when the observations are captured at non-equidistant intervals. Consequently, the framework can adapt to the granularity of the observations and provide exact probabilistic predictions at any resolution.

Each of these properties can be realized if we take the latent processes to be a function of

independent Gauss–Markov processes [34] with background-driving, non-Gaussian Lévy processes [26, 27]. The Gauss–Markov processes $\kappa_k^m(t)$ are the solutions of the stochastic difference equation $\mathrm{d}\kappa_k^m(t)^2 = -\lambda_k^m \kappa_k^m(t)^2 \mathrm{d}t + \mathrm{d}z_k^m(t\lambda_k^m)$. Here, λ_k^m is a positive scalar delay parameter and $z_k^m(t)$ is a non-Gaussian Lévy process for the mth motion primitive and kth data modality. We assume that the Lévy process has positive increments and no drift, which means that the Gauss–Markov process will be positive.

We can give an intuitive explanation for the behavior of a Gauss–Markov process. It is a process that moves up entirely by incremental jumps and then tails off exponentially according to the decay parameter. The use of the Lévy process implies that the timing of the jumps is random. This behavior is similar to the switching diffusion process of Liechty and Roberts [35]. Despite the relatively simple dynamics, our simulation results indicate that combinations of Gauss–Markov processes should be capable of describing hydromedusae movements.

We employ the Gauss–Markov processes in a generative model [36]. The generative model encodes our prior assumptions about the kinematics dynamics and determines how the hydromedusae movements could have been generated based upon those priors

$$\begin{aligned}
&\mathrm{d}y_k^m(t;\, p) \sim -a_k^m\left(y_k^m(t) - b_k^m\right)\mathrm{d}t \\
&\quad + \kappa_k^m(t)^{1/2}\mathrm{d}B_k^m(t), \\
&\kappa_k^m(t)^2 \sim \textsc{Gauss–Markov Process}\left(z_k^m,\, \lambda_k^m\right), \\
&B_k^m \sim \textsc{Brownian Motion}, \\
&z_k^m \sim \textsc{Lévy Process}\left(\nu_k^m,\, \psi_k^m,\, \mathcal{K}_k\right). \qquad (1)
\end{aligned}$$

Here, a_k^m is a variable that determines the rate at which the dynamics evolve, with larger values indicating increasingly frequent changes. As well, b_k^m is a vector that controls the mean value of the dynamics in multiple dimensions. For the Lévy process, ν_k^m and ψ_k^m are, respectively, the mass and decay terms, while $\mathcal{K}_k$ is the base measure for the process.

This generative model is the simplest case of how we will describe the kinematics dynamics of the motion primitives. It essentially says that the kinematics come from a single Gauss–Markov process. While model (1) may be sufficient for some types of actions, it will not be for all of actions that we consider here. This is because some of the hydromedusae movement sequences may not be adequately described by only one Gauss–Markov process. We therefore build up to a more suitable model, given in (4), that aggregates multiple Gauss–Markov processes. Toward this end, we start by re-writing the Gauss–Markov process as a transformation of a Poisson process [37]

$$\begin{aligned}
&\mathrm{d}y_k^m(t;\, p) \sim -a_k^m\left(y_k^m(t) - b_k^m\right)\mathrm{d}t \\
&\quad + \kappa_k^m(t)^{1/2}\mathrm{d}B_k^m(t), \\
&\kappa_k^m(t)^2 \sim \exp\left(-\lambda_k^m t\right)\kappa_k^m(0)^2 \\
&\quad + \sum_{j=1}^{\infty} \exp\left(\tau_{j,k}^m \lambda_k^m\right)\int_{\alpha_{j,k}^m/t\lambda_k^m}^{\infty} z_k^m(w)\,\mathrm{d}w, \\
&B_k^m \sim \textsc{Brownian Motion}, \\
&z_k^m \sim \textsc{Lévy Process}\left(\nu_k^m,\, \psi_k^m,\, \mathcal{K}_k\right), \qquad (2)
\end{aligned}$$

where $\{\alpha_{j,k}^m\}_{j=1}^{\infty}$ and $\{\tau_{j,k}^m\}_{j=1}^{\infty}$ are two independent sequences of random variables corresponding to the arrival times of a Poisson process with unit intensity. It is important to note that the transformation from (1) to (2) is not an approximation, which means that the behavior of (2) is the same as (1). This is because a Poisson process is a special case of the Lévy process: it characterizes the number of jumps performed by the Lévy process.

If the background-driving Lévy process is a compound Poisson process, then the Gauss–Markov process in (2) can be converted from a Poisson process to the limit of a marked point process [38],

$$\begin{aligned}
&\mathrm{d}y_k^m(t;\, p) \sim -a_k^m\left(y_k^m(t) - b_k^m\right)\mathrm{d}t \\
&\quad + \sum_i \kappa_{i,k}(t)^{1/2} dB_k^m(t), \\
&\kappa_{i,k}^m(t)^2 \sim \sum_{i=1}^{\infty}\sum_{j=1}^{\infty} \exp\left(-t\lambda_k^m + \lambda_k^m \tau_{i,j}\right) \\
&\quad \times J_{i,j}\delta_{\tau_{i,j}<t}, \quad B_k^m \sim \textsc{Brownian Motion}. \qquad (3)
\end{aligned}$$

Here, $J_{i,j}$ are the random samples of a Poisson jump distribution. The delta symbol corresponds to the indicator function: $\delta_{\tau_{i,j}<t} = 1$ when $\tau_{i,j} < t$.

The dynamics modeling formulation in (3) proves to be useful for our purposes. It is advantageous because (3) contains a superposition of Gauss–Markov processes, the limit of which can mimic virtually any deterministic or stochastic phenomena. More specifically, the model assumes that the kinematics phase space can be segmented into regions of variable scale, with each region characterized by a Gauss–Markov process. When each region has infinitesimal size, the dynamics become trivial to describe. As the size of the regions increases, the dynamics can become more complicated. Properties of the Gauss–Markov processes [29, 30] ensure that (3) can tolerate some complexity in the dynamics.

It is often difficult to choose a suitable number of Gauss–Markov processes for representing the kinematics dynamics. We therefore have adopted a nonparametric assumption [32] in (3): there potentially is an infinite number of Gauss–Markov processes in the superposition, a finite number of which will have non-negligible weight. The number of Gauss–Markov processes will be automatically discerned by our inference scheme.

Additional priors need to be imposed to complete the model in (3). Toward this end, we assume that the masses of the Poisson process are the jumps of a

Gamma process. The decay parameters of the Poisson process are independently and identically distributed according to a base distribution. We do not have an explicit form in mind for the jump distribution of the Poisson process. As such, we utilize a Polyá tree prior [39, 40],

$$
\begin{aligned}
&x_k^m(t) \sim \sum_{p=1}^{P} w_k^m(t) P_k^m y_k^m(t;\, p) + \sigma_k^m(t),\\
&P_k^m \sim \text{Normal Diffuse}\left(a_p,\, b_p\right),\\
&\sigma_{l,k}^m \sim \text{Normal}\left(a_\sigma,\, b_\sigma\right),\\
&\mathrm{d}y_k^m(t;\, p) \sim a_k^m\left(y_k^m(t) - b_k^m\right)\mathrm{d}t\\
&\quad + \sum_i \kappa_{i,k}(t)^{1/2}\mathrm{d}B_k^m(t),\\
&\kappa_{i,k}^m(t)^2 \sim \text{Marked Point Process}\left(\vartheta_{i,j',k}^m,\, \tau_{i,k}^m,\, \lambda_{i,k}^m\right),\\
&\tau_{i,k}^m \sim \text{Poisson Process}\left(\nu_{i,k}^m,\, \psi_{i,k}^m\right),\\
&\vartheta_{i,j',k}^m \sim \text{Pólya Tree}_{j'}\left(g_k^m,\, \sigma_k^m,\, \mathcal{Q}_{k;\vartheta}^m\right),\\
&B_k^m \sim \text{Brownian Motion},\\
&\nu_{i,k}^m \sim \text{Gamma Process}\left(\varsigma_k^m\right), \quad \psi_{i,k}^m \sim \mathcal{H}_k.
\end{aligned}
\tag{4}
$$

The use of these priors does not change the core behavior of (3): (4) represents the hydromedusa kinematics as a sum of Gauss–Markov processes with comparatively simple dynamics. One difference, however, is that (4) offers a rigorous way for our inference scheme to choose various parameter values based upon the sequences of hydromedusa movement observations. That is, we will allow the observations to define possible parameter values versus forcing investigators to explicitly choose them. Automating the parameter selection helps guarantee that the dynamical pattern generators will accurately track the hydromedusa movement trajectories. It also requires less manual intervention from investigators.

Another difference between (3) and (4) is that (4) provides a relationship between the hydromedusae motion observations and the movement dynamics. In (4), we assume that the observations $x_k^m(t)$ at time t are a weighted projection of latent processes $y_k^m(t;\, p)$. This projection is performed so that the latent processes can be efficiently evaluated. The number of latent processes chosen by our inference scheme to characterize the observations are taken as the number of motion primitives.

To implement the model in (4) for practical purposes, a robust inference scheme is needed to deduce the distributions associated with the parameters. Hence, we look to two Markov chain Monte Carlo samplers (see the appendix for the mathematical details). The first is furnished for batch training [41]. Batch training is commonly performed when all of the data to describe some phenomena has been collected. The second sampler serves in a broader online setting [42], which is invaluable when there is an initial lack of data and more observations are added over time. The latter of these inference schemes can be combined with the predictive uncertainties returned by the model. These uncertainties signify when the learned dynamical systems will no longer be well-aligned with the motions being captured and thus must be updated if they are to remain relevant.

3. Experiments and analysis

We have two goals for the ensuing experiments on motion sequences from *S. tubulosa* and *A. victoria*. The first is to determine if the segmentation boundaries are defined when there are gradual or abrupt changes in either localized or widespread bodily motion (see sections 3.2.1 and 3.3.1). If so, then these primitives can be strung together and be useful for control of a soft-body platform. This is because they should correspond with changes in actuation regimes. Secondly, we would like to establish what effect each primitive has on the locomotion dynamics (see sections 3.2.2 and 3.3.2). With this information, we can identify where improvements might be made in the motions. Actually improving the motion primitives will be the subject of our future endeavors.

Before we discuss our experimental protocols and the results, we provide a review of pressure and circulation in hydromedusae locomotion (see section 3.1). This discussion provides context for the ensuing analysis.

3.1. Pressure and circulation in hydromedusae locomotion

The locomotion of marine animals in general relies on pressure forces generated by transferring hydrodynamic impulse to the surrounding fluid. For jellyfish, the impulse is transfered in the form of a propulsive jet. In [43], Krieg and Mohseni derived an analytical model for the pressure inside of jetting cavities which can be utilized to correlate the relationship between the different motion primitives and the propulsive performance. This model integrates the momentum equation from a farfield location along a strategic path, taking into account symmetry conditions, in order to relate pressure on the body to pressure at stagnation, P_∞. Unknown velocity integrals which appear during this process are then correlated to the total circulation of certain characteristic regions. The pressure at the location on the jellyfish cavity surface intersecting the axis of symmetry, P_b, is shown to be proportional to the rate of change of circulation in both the cavity and the jet region,

$$
\frac{P_b}{\rho} = \frac{P_\infty}{\rho} + \frac{\mathrm{d}\Gamma_{\text{Jet}}}{\mathrm{d}t} + \frac{\mathrm{d}\tilde{\Gamma}_{\text{Cav}}}{\mathrm{d}t} + \frac{1}{2}u_b^2.
$$

In this equation u_b is the velocity of the jellyfish surface at the location where the pressure is determined, ρ is the fluid density, Γ_{Jet} is the circulation in the jet region (anything downstream of the velar opening), and $\tilde{\Gamma}_{\text{Cav}}$

Table 1. A summary of the geometry, physical, and flow characteristics for motion primitives of *S. tubulosa*.

Phase	Geometry/physical change	Flow effects
Pressurize	There is an outward rotation of the velar flap and a pressurization of the subumbrellar cavity. Half-sink terms dominate.	The outward flow across the velum increases sharply.
Jet formation	The bell compresses and the velar flap continues to rotate outward. An increase in pressure is seen due to vorticity flux. The power is maximized.	An ejecting jet is formed. The fluid slug begins to be ejected in this phase.
Jetting	The minimum velar diameter and bell volume are achieved. The maximum bell pressure and upstream thrust are achieved.	Propulsive vortex ring formation, separation, and translation occurs. The remainder of the ejected fluid slug is moved into the ring before separation.
Refill	The cavity volume and velar diameter increase. An upstream thrust is generated due to the relaxation vortex striking the cavity.	There is an inward flow of fluid, which refills the subumbrellar cavity. A relaxation vortex is also formed inside the cavity.
Coasting	There are slight velar oscillations due to small pressure changes.	There are slight inward and outward flow changes across the velum. The relaxation vortex diffuses.

is the circulation within the subumbrellar cavity not including circulation due to cavity surface stretching. In addition the circulation dynamics of both regions can be broken down into four basic components: vorticity flux, half-sink flows, boundary deformation, and vortex impingement, which we will summarize briefly. As fluid is ejected out of, or into, a cavity it carries with it a free shear tube which rolls into a vortex ring. The growing shear layer in the jet region corresponds to the vorticity flux circulation which we refer to as Γ_{VF}. The rate at which this circulation grows is proportional to the square of the jet velocity,

$$\frac{d\Gamma_{VF}}{dt} = \frac{1}{2}\bar{u}^2 K_{VF},$$

where $\bar{u}$ is the average jet velocity, $\bar{u} = \dot{\Omega}/\pi R^2$, and K_{VF} is a vorticity flux constant which takes into account increased rates of circulation flux due to both boundary layer development on the nozzle and radial velocity components, which is characterized for multiple nozzle geometries in [44]. Whenever fluid is forced through a finite opening a jet is formed on one side carrying vorticity with it in a detached shear layer. On the other side the fluid converges to fit through the opening. At a great distance this flow looks identical to one side of a point sink. Krieg and Mohseni [43] demonstrated that the flow inside a cavity during jetting (or outside the cavity during refilling) can be effectively modeled by that of a finite area circular sink plate, bisected by the opening plane, with total strength equal to the volume flux. The circulation of such a flow, Γ_{HS}, is described in great detail in [43] for those interested, here we just summarize the growth rate.

$$\frac{d\Gamma_{HS}}{dt} = K_{HS}\frac{\ddot{\Omega}R - \dot{\Omega}\dot{R}}{R^2}$$

Here, K_{HS} is a constant related to the half-sink circulation which depends on the velocity boundary conditions in the plane which extends radially outward from the velar opening. If the velocity is restricted by a solid boundary, $K_{HS} = 0.34$, and if the boundary is free, $K_{HS} = 0.15$.

The circulation due to vortex ring impingement is more difficult to summarize in such a concise manner. As the jellyfish expands refilling the subumbrellar cavity, the shear layer accompanying the incoming fluid rolls into a vortex ring much like the jet flow, but the ring must remain confined to the cavity region. As the vortex approaches the inner walls a boundary layer of opposite vorticity forms on the cavity surface from the discontinuity between vortex induced velocity and the no slip condition. The growth of the impingement boundary layer counteracts the circulation flux at the opening, but the exact magnitude of the impingement circulation depends on the exact geometry of the boundary, and the strength/size of the internal vortex ring. The circulation due to boundary deformation does not directly affect the reference pressure dynamics. From this methodology it can be seen that jet acceleration and changes in opening radius affect the pressure through the half-sink circulation terms; whereas, the magnitude of the jet velocity affects the pressure through the vorticity flux circulation terms.

3.2. *Sarsia tubulosa* results and discussion

Our experiments for *S. tubulosa* (M. Sars, 1835) used a hydromedusa with a maximum and minimum bell radius of 0.63 and 0.57 cm, respectively. Additionally, the subumbrellar volume had a maximum value of approximately 0.45 cm^3 and a minimum value of 0.26 cm^3.

The bell deformations for *S. tubulosa* were determined from videos of physical specimens previously utilized in [2]. As a summary, the hydromedusa was placed within a vessel of sufficient size to permit free swimming. The organism was illuminated via a planar laser directed through the central axis. Fluorescein dye was also injected to enhance the illumination. After video capture, the body was manually delineated in each frame and approximated using basis splines. Fourier-time-series interpolation was employed as a post processing step to create numerical models of the periodic contractions.

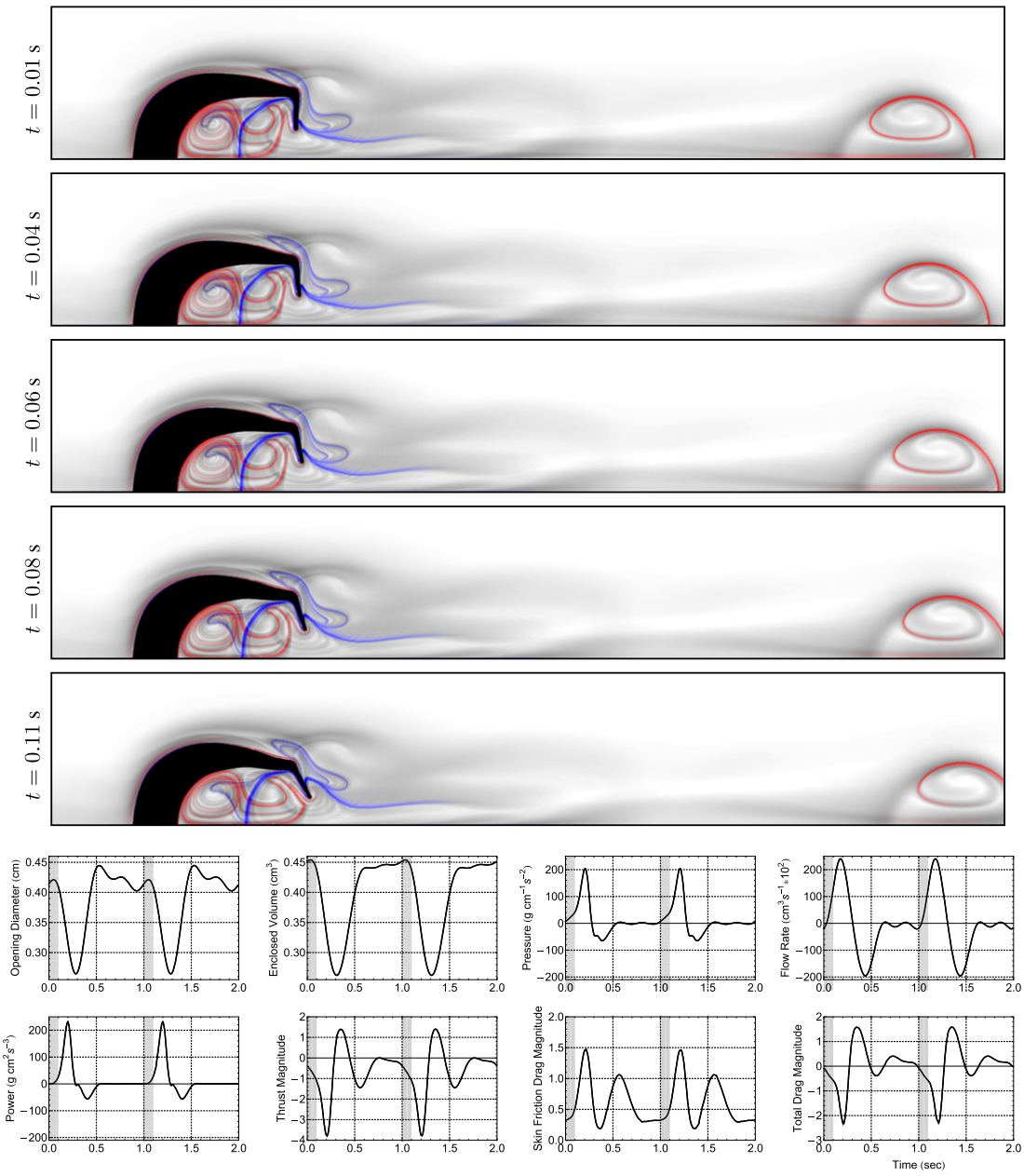

Figure 1. The first motion primitive, pressurization, for *S. tubulosa*, where the velar flap extends downstream and the bell compresses. (top) Plots of the Lagrangian coherent structures for five near-equally spaced time steps over the duration of the primitive ($t = 0.01,\ 0.04,\ 0.06,\ 0.08,\ 0.11$ s). Since the jellyfish is axisymmetric, we show only two-dimensional plots. In these plots, blue curves represent the forward structures and the red curves represent the backward structures. Mixtures of the forward and backward structures are given in gray, where the whiter values denote lower-magnitude transport. The bell of the hydromedusa is displayed in black. (bottom) Plots of the velar diameter, subumbrellar volume, cavity pressure, flow rate, power output, thrust coefficient, total drag, and skin friction. In these plots, the gray shaded region denotes the time in which the motion primitive takes place. Since the propulsive motion was cyclic, we have plotted two periods.

As mentioned above, our generative model automatically determines the number of motion primitives in an observation set. When applying the model to a single swimming cycle, it returned a total of five primitives, summaries of which are provided in table 1. The motion subsequences defined by these primitives are displayed in figures 1–5; for each subsequence, we plotted the motion at five equally spaced time steps. To emphasize the effect that these motions have on the surrounding fluid, we overlaid the associated two-dimensional Lagrangian coherent structures (LCS) [45, 46]. For these plots and those to come, the LCS are visualized as ridges of the finite-time Lyapunov exponent field. The forward coherent structures denote particle advection forward in time and represent regions where the particles diverge quickly. The backward coherent structures correspond to particle advection in the past and outline attracting or converging flow regions. Thus, LCS represent transport barriers with negligible surface normal flux and therefore dictate fluid transport and mixing. We computed the LCS from the velocity fields returned by a Navier–Stokes solver using an arbitrary Lagrangian–Eulerian method [2, 47].

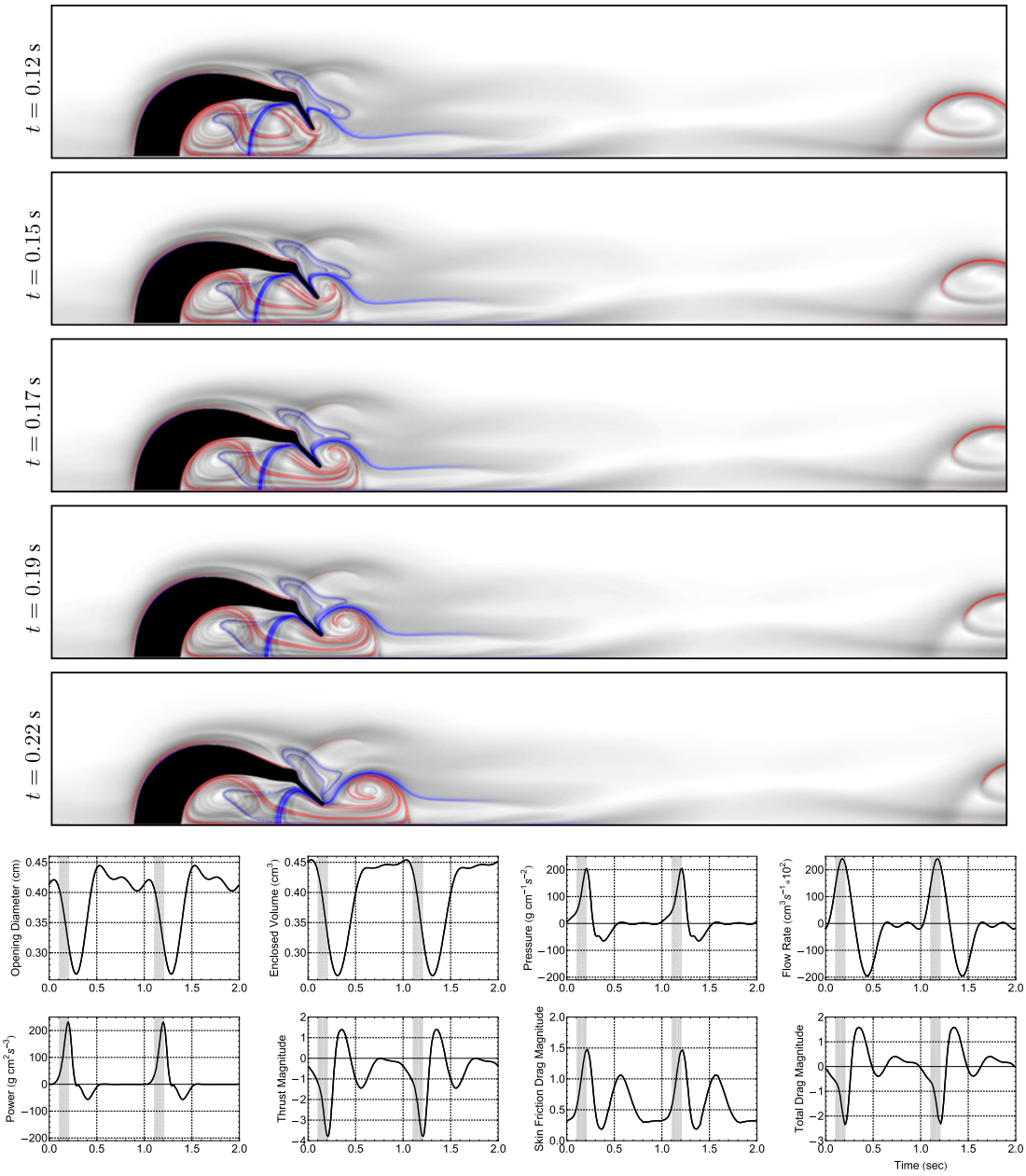

Figure 2. The second motion primitive, jet formation, for *S. tubulosa*, where a nozzle-like mechanism is formed and a jetting-based vortex is produced. (top) Plots of the Lagrangian coherent structures for five near-equally spaced time steps over the duration of the primitive ($t = 0.12$, 0.15, 0.17, 0.19, 0.22 s). Since the jellyfish is axisymmetric, we show only two-dimensional plots. In these plots, blue curves represent the forward structures and the red curves represent the backward structures. Mixtures of the forward and backward structures are given in gray, where the whiter values denote lower-magnitude transport. The bell of the hydromedusa is displayed in black. (bottom) Plots of the velar diameter, subumbrellar volume, cavity pressure, flow rate, power output, thrust coefficient, total drag, and skin friction. In these plots, the gray shaded region denotes the time in which the motion primitive takes place. Since the propulsive motion was cyclic, we have plotted two periods.

The velocity vector fields that we use come from the previous work in [47]. In [47], Sahin and Mohseni developed a fluid solver that relies on an arbitrary Lagrangian–Eulerian [48] formulation of the Navier–Stokes equations. This formulation is applicable to moving boundary problems that can be represented in swirl-free cylindrical coordinates. Assessing the flow around deforming hydromedusae bodies is an example of such a problem. From properties of the fluid flow, it will be possible to estimate various dynamics quantities, such as the power output into the surrounding fluid, skin friction drag, and the internal cavity pressure. We use these dynamics quantities when assessing the motion primitive segmentations. In particular, we show that the motion primitive breakpoints are well aligned with trend changes in the dynamics. This finding implies that we have defined a meaningful temporal segmentation of the hydromedusa body movements.

In the solver, an unstructured, derformable mesh is employed to follow the interface between the simulated fluid and the hydromedusa body. The mesh for

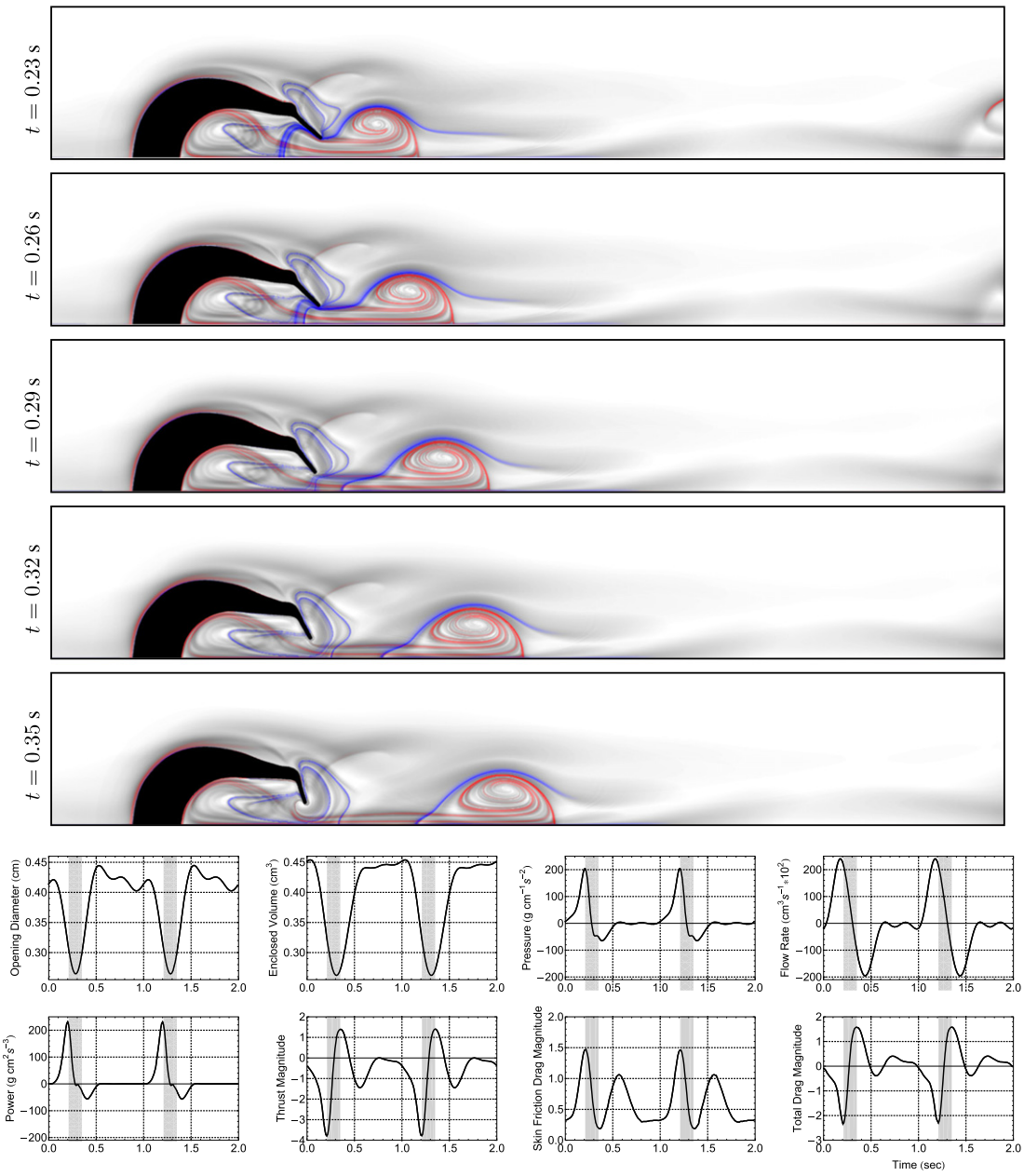

Figure 3. The third motion primitive, jetting, for *S. tubulosa*, where the vortex is pinched off and the velar flap retracts. (top) Plots of the Lagrangian coherent structures for five near-equally spaced time steps over the duration of the primitive ($t = 0.23,\ 0.26,\ 0.29,\ 0.32,\ 0.35$ s). Since the jellyfish is axisymmetric, we show only two-dimensional plots. In these plots, blue curves represent the forward structures and the red curves represent the backward structures. Mixtures of the forward and backward structures are given in gray, where the whiter values denote lower-magnitude transport. The bell of the hydromedusa is displayed in black. (bottom) Plots of the velar diameter, subumbrellar volume, cavity pressure, flow rate, power output, thrust coefficient, total drag, and skin friction. In these plots, the gray shaded region denotes the time in which the motion primitive takes place. Since the propulsive motion was cyclic, we have plotted two periods.

S. tubuolsa consists of 182 517 vertices and 181 730 quadrilateral elements. The mesh for *A. victoria* consists of 205 714 vertices and 204 784 quadrilateral elements. These meshes are stretched next to the hydromedusa bell surfaces to resolve the viscous flow within the boundary layer.

The governing equations for the viscous fluid flow are discretized on the meshes using the dilation-free, semi-staggered finite volume method given in [49]. In addition to solving the incompressible Navier–Stokes equations, the equations of motion for a deforming body are simultaneously solved in a fully-coupled form. The underlying mesh is deformed by solving the linear elasticity equation at each time level. This is done using GMRES method [50] with the restricted, additive Schwarz preconditioner and the inverse-LU-decomposition preconditioner with reverse Cuthill–McKee ordering. Remeshing is avoided to enhance the

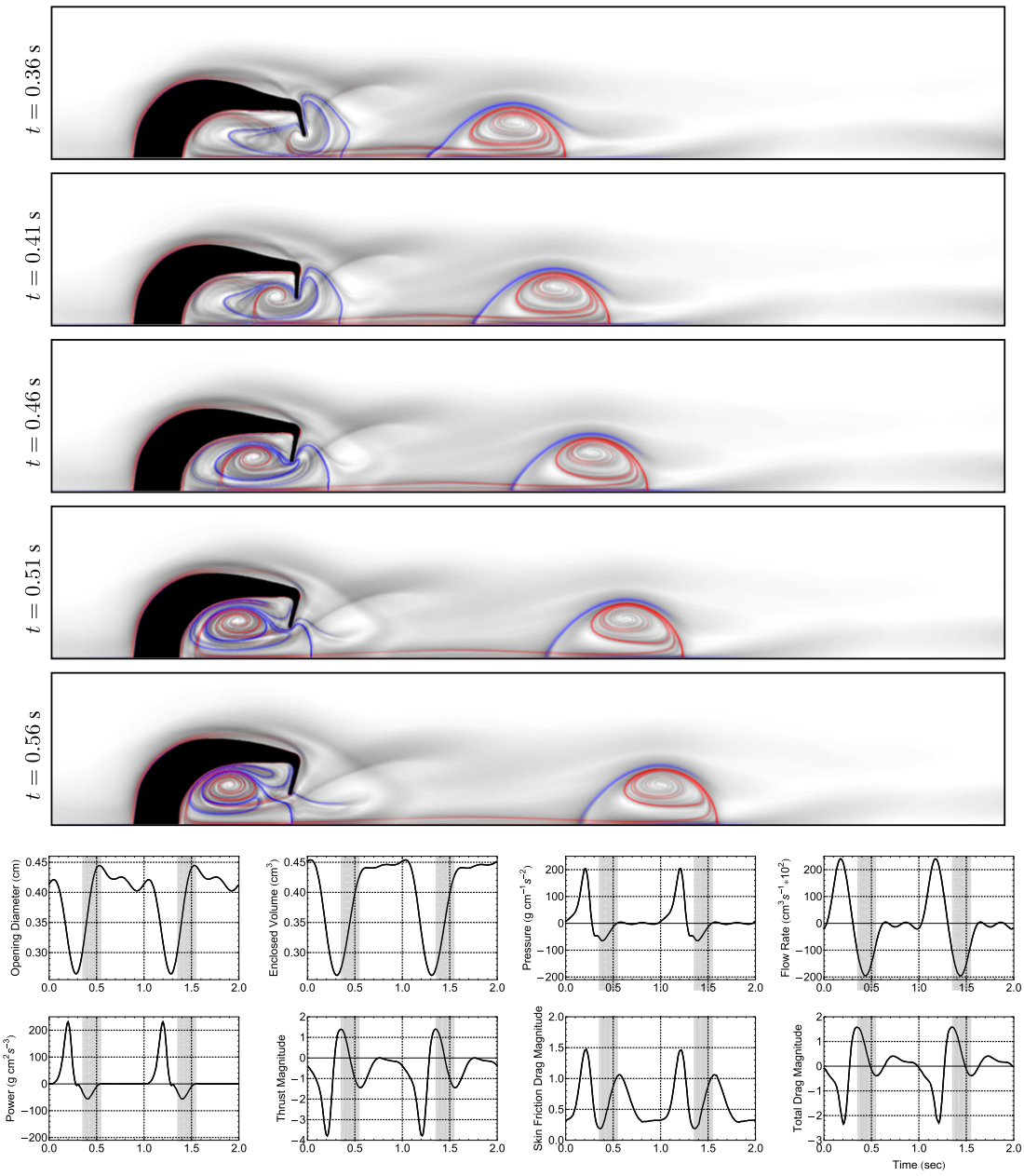

Figure 4. The fourth motion primitive, refill, for *S. tubulosa*, where the bell expands and creates a stopping vortex inside the subumbrellar cavity. (top) Plots of the Lagrangian coherent structures for five near-equally spaced time steps over the duration of the primitive ($t = 0.36,\ 0.41,\ 0.46,\ 0.51,\ 0.56$ s). Since the jellyfish is axisymmetric, we show only two-dimensional plots. In these plots, blue curves represent the forward structures and the red curves represent the backward structures. Mixtures of the forward and backward structures are given in gray, where the whiter values denote lower-magnitude transport. The bell of the hydromedusa is displayed in black. (bottom) Plots of the velar diameter, subumbrellar volume, cavity pressure, flow rate, power output, thrust coefficient, total drag, and skin friction. In these plots, the gray shaded region denotes the time in which the motion primitive takes place. Since the propulsive motion was cyclic, we have plotted two periods.

robustness of the solver and improve its computational efficiency [51].

3.2.1. Evaluating hydromedusa motions and their flow fields

Stepping through the plots in figure 1, the first motion primitive, which we call the pressurization primitive, corresponds to a single motion occurring over a span of 0.11 s. The first motion primitive is an outward rotation of the velar flap, which causes it to protrude in the downstream (left-to-right) direction. Given the current knowledge of neuromuscular systems in hydromedusae [52], we believe that this movement is a reaction to the pressurization of the subumbrellar cavity relative to the outside fluid. That is, slight changes in the cavity volume initiate rapid pressure changes, which is due the fact that the fluid is incompressible. Also note that many hydromedusae lack sufficient motor control to explicitly move the velar flap.

This bodily deformation corresponds to the beginning of fluid expulsion from the subumbrellar cavity.

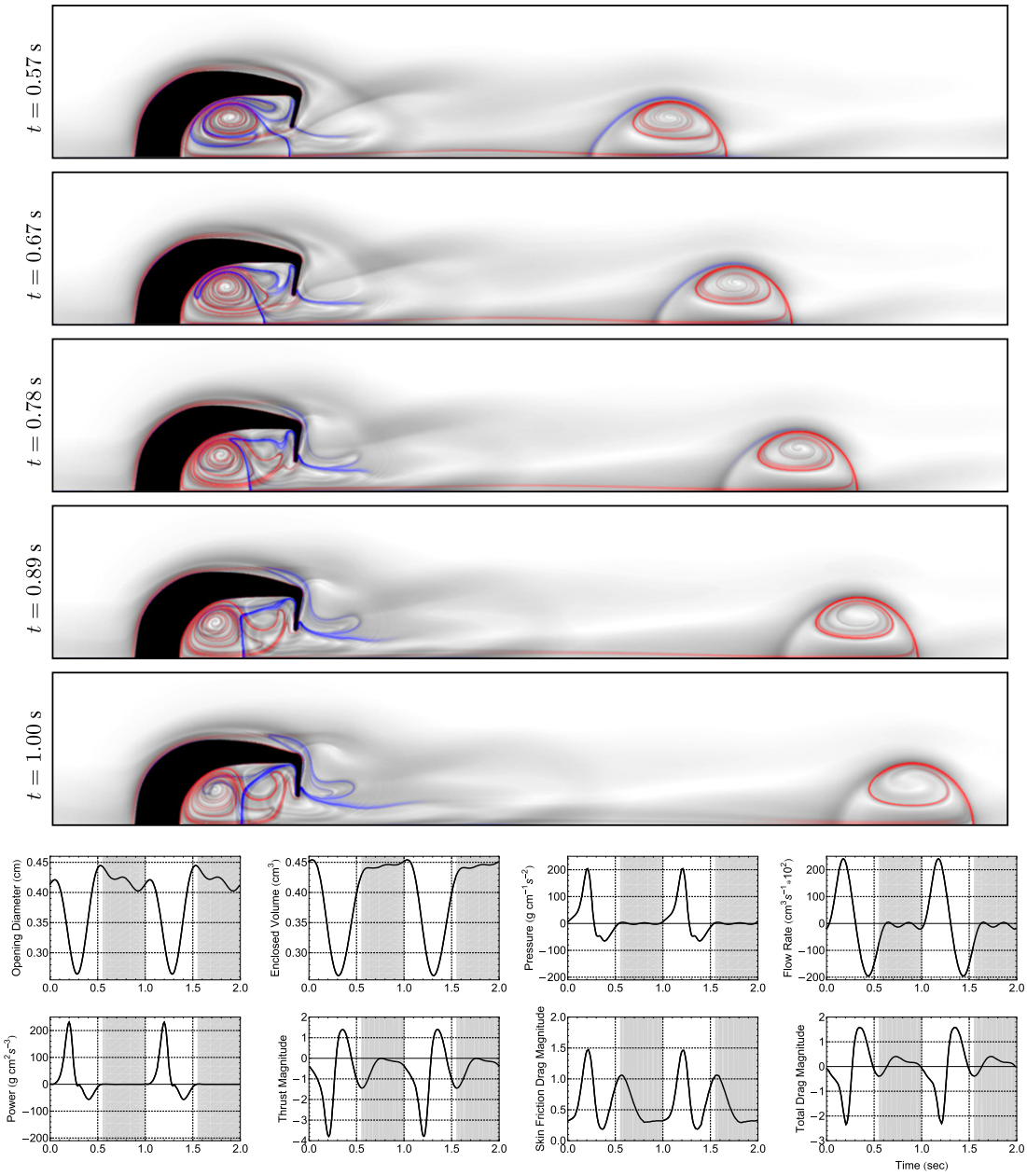

Figure 5. The fifth motion primitive, coasting, for *S. tubulosa*, which is a coasting phase. (top) Plots of the Lagrangian coherent structures for five near-equally spaced time steps over the duration of the primitive ($t = 0.57$, 0.67, 0.78, 0.89, 1.0 s). Since the jellyfish is axisymmetric, we show only two-dimensional plots. In these plots, blue curves represent the forward structures and the red curves represent the backward structures. Mixtures of the forward and backward structures are given in gray, where the whiter values denote lower-magnitude transport. The bell of the hydromedusa is displayed in black. (bottom) Plots of the velar diameter, subumbrellar volume, cavity pressure, flow rate, power output, thrust coefficient, total drag, and skin friction. In these plots, the gray shaded region denotes the time in which the motion primitive takes place. Since the propulsive motion was cyclic, we have plotted two periods.

The LCS corroborate this claim, as the backward (red) LCS near the velum moves in the downstream direction and begins to show a counter-clockwise rotation. This LCS will form the leading edge of the vortex that will form from fluid ejected during the contraction occurring in the second primitive. Additionally, the forward (blue) LCS that extends downstream outside the bell reveals the boundary of the fluid region that will be entrained into the vortex. The forward LCS within the bell defines the trailing edge of the fluid that will be ejected in the vortex.

The second motion primitive, shown in figure 2, continues the same action seen in the first primitive, albeit more visually pronounced. As well, the bell contracts, creating a nozzle-like velar profile [53]. The quick combination of these two actions precipitates the ejection of fluid and development of a propulsive starting vortex. We therefore refer to this primitive as jet formation. As the LCS show, fluid is being expelled from the subumbrellar cavity and the start of vortex formation is clearly seen in the rollup of the backward LCS. The most prominent forward LCS within the

cavity moves toward the velar opening, marking the boundary between fluid that will be ejected into the forming vortex and that which will be left behind.

There are two other notable fluid structures present during the pressurization and jet formation motion primitives. Foremost, there is fluid circulating clockwise within the subumbrellar cavity, which is due to the relaxation vortex that forms while fluid is drawn into the bell during the coasting phase from the previous swimming cycle. This is most evident in the backward LCS during the first motion primitive. In the jet formation motion primitive, these structures begin to dissipate due to viscous decay of circulation. Secondly, a closed lobe formed by a forward LCS near the rear of the hydromedusa begins to sharpen and morph. This lobe is adjacent to the velar flap and contains fluid that will eventually be entrained into the cavity.

The third motion primitive, shown in figure 3, is nearly a reversal of the first and second primitives: the velar flap rotates clockwise and the hydromedusa bell expands outward by a marginal amount over 0.13 s. The velar flap retracts due to the fact that subumbrellar pressurization has ceased and because the vortex separates from the hydromedusa and begins to move downstream. This primitive will be known as jetting. As the vortex moves downstream, the forward LCS near the velum moves into the subumbrellar cavity. This LCS highlights fluid that will be pulled into the bell during the ingestion or refilling phase of swimming. As the propulsive vortex moves downstream, it continues to draw in surrounding fluid and increase in size until the vortex reaches a more steadily translating phase. Fluid enters the vortex through the gap between the forward and backward LCS at the top of the vortex. This additional fluid also acts to slow the vortex motion, since momentum must be conserved.

The fourth motion primitive corresponds to the refilling phase of the hydromedusa's swimming cycle. This motion primitive, shown in figure 4, consists of an inward rotation of the velar flap and an expansion of the subumbrellar cavity. This motion primitive has a duration of 0.21 s and mostly corresponds to an expansion of the hydromedusa's bell. There is no musculature present to induce this motion, so it is caused by the elastic strain energy stored in the bell structures during the contraction phase [8]. The rapid expansion of the bell quickly draws fluid into the subumbrellar region, generating a relaxation vortex within the bell. This is clearly seen in the LCS in figure 4. This relaxation vortex is difficult to evaluate since it resides within the subumbrellar cavity. Its existence was first quantified numerically by Lipinski and Mohseni [10] and experimentally by Krieg and Mohseni [43].

The fifth motion primitive corresponds to a passive coasting phase, as seen in figure 5. There are small oscillations present in the velar flap due to elastic and pressure effects, but there are no major body motions taking place during this time. The ejected starting vortex continues to move downstream and gradually decays, while the newly generated relaxation vortex also decays within the subumbrellar cavity.

3.2.2. Evaluating hydromedusa motions and dynamics quantities

As we have demonstrated, each motion primitive for the *S. tubulosa* is correlated with transitions between distinct, fluid-influencing movements. The primitives can additionally be connected with meaningful changes in the surrounding fluid environment, despite not explicitly accounting for such information in the segmentation process. This connection is due to the direct influence of the body motion on the surrounding fluid. That is, hydromedusa have developed their body motions in order to swim effectively, which results in large fluid momentum transfer for a given motion.

In this section, we consider the relationship between the motion primitives and several properties of the fluid surrounding the hydromedusa. As mentioned at the beginning of this section, the pressure dynamics can be related to three basic components of the system circulation [43]. These components are observed to have drastically different relationships with the subumbrellar cavity volume and the velar opening diameter, which are shown in figures 1–5. We expect changes in body motions, denoted by the different motion primitives, to relate to changes in the different circulation components, even though there is usually not a direct correspondence.

During the pressurization primitive, there is little change in the volume and diameter measurements, although both begin to decrease by the end of this primitive due to the ongoing bell contraction. Even though the volume flux is small during this primitive, the rate at which the volume flux increases is substantial. This implies that the cavity circulation during this primitive is dominated by half-sink components, driving the initial cavity pressurization.

In the jet formation primitive, the cavity volume and opening diameter rapidly decrease as fluid is expelled from the bell. During this primitive the pressure dynamics are dominated by the vorticity flux components in the jet due to the large jet velocities. The half-sink components continue to aid in pressurization with continual increase in volume flux. The jetting motion primitive captures the end of the contraction phase and both the velar diameter and the subumbrellar volume reach their minimum values during this time. The jetting primitive marks when the volume flux begins to decrease and the contribution to total circulation from the half-sink components opposes the contributions from vorticity flux. As such the pressure reaches a maximum at the transition between the jet formation and jetting primitives. At the onset of the jetting primitive, the vorticity flux still dominates. Toward the end of the jetting primitive, the reduced volume flux greatly reduces contributions from these

components. The half-sink components eventually become dominant, resulting in the negative pressure force at the end of this primitive

During the refill primitive, the bell expands, rapidly drawing in fluid and increasing the subumbrellar volume. As the bell expands, the velar diameter also increases until both quantities are near their starting values. The refill motion primitive contains all circulation generating components, but it is not dominated by any one component. At the onset, the increase in incoming volume flux creates a half-sink flow in the jet. This half-sink flow compliments the vorticity flux circulation in the cavity and results in the small negative pressure peak. However, as the inward volume flux increases and the vorticity flux components become substantial, the internal vortex ring also impinges on the inner surfaces generating opposing circulation in the attached boundary layer. This event contradicts the effects of the vorticity flux components. Towards the end of the refill primitive, the impingement circulation and the internal ring reach an equilibrium state. Any remaining generation of circulation due to vorticity flux is canceled out by the half-sink term in the jet. The jet has changed sign due to the now decreasing inward volume flux. The volume continues to very slowly increase during the fifth motion primitive, which represents the coasting phase of swimming. However, the volume flux rate is minimal. During the coasting primitive, there is no significant generation of circulation due to the body motion. Rather, the circulation during this primitive is dominated by viscous dissipation, which does not directly affect pressure forces the way that active generation of circulation does.

Because the *S. tubulosa* propels itself via jets created by pressurizing the subumbrellar cavity, we can easily estimate three other quantities. These quantities are the power output due to the jet through the velar opening, the average cavity pressure along the subumbrellar surface, and the flow rate through the velar opening [10]. As seen in figures 1–5, the segmentation boundaries are linked with slope changes and inflection points in the power output and cavity pressure. For the pressurization motion primitive, the power and pressure both rise, since some amount of positive work is being done to begin the contraction phase. During the jet formation primitive, this rate increases dramatically as the vortex is ejected from the subumbrellar cavity. Both the cavity pressure and the power output peak as the vortex begins to separate from the cavity in between the jet formation and jetting primitives. As was mentioned previously, the peak in pressure coincides with the peak velocity/vorticity flux and the reversal of the half-sink circulation as volume flux begins to decelerate. The peak power occurs similarly at this time, as discussed in [43]. This is because the vorticity-flux-dominated peak pressure also coincides with the peak body surface velocity required to create the large volume changes. The lowest values for the power, cavity pressure, and flow rate occur in the refill primitive as the bell expands, drawing fluid into the bell and generating a slight negative thrust and power. During the coasting primitive, the velum undulations cause the pressure to oscillate slightly, but the power output from the cavity is essentially zero during this time. That is, the hydromedusae is not performing meaningful work.

Unlike the power output and cavity pressure, the flow rate inflections are not well correlated with the remaining dynamics. We believe that there are two sources to this discrepancy. First, although the fluid might be accelerating or decelerating in a particular direction over the course of a primitive, the fluid velocity will not be altered instantaneously. Thus, the alterations brought on by one primitive may persist in the next. Secondly, most of the primitives embody compound movements, which may have a complex influence on certain variables.

A somewhat surprising finding is that the breakpoints closely matched trends in thrust, skin friction drag, and total drag [2] for figures 1–5. After analysis, we determined that the reasoning for these relationships is similar to that of power and cavity pressure, so we will not discuss it in detail. The effect of vortex ring impingement can be seen to a much greater degree in the total thrust of the refill primitive, almost completely negating the negative thrust caused by vorticity flux into the cavity during refilling. Similarly the power output becomes negative during the refill primitive as fluid begins to do work on the jellyfish body through impingement.

There is some physical significance to the inflection points of the thrust and drag: the last four breakpoints begin when the jounce is zero. Jounce, which is also referred to as snap, is the second time derivative of acceleration and the first time derivative of jerk. Qualitatively, it is a gauge of how frequently a force is being applied and removed. Therefore, we can think of the breakpoints as being small-scale time periods where there is a constant force being applied to the surface of the velar opening. Phrased differently, the breakpoints are defined when there appears to be a progression from one flow pattern to another.

Due to this clear segregation of the forces and flows, it is our belief that there should be (near-)seamless transitions between motion primitives for certain types of maneuvers. We speculate that these transitions between maneuvers would not greatly degrade propulsion efficiency. If the breakpoints were specified elsewhere throughout the cycle, it is plausible that a bio-inspired platform would have to expend unnecessary effort to counteract a mixture of inhibiting forces. For example, if the second motion primitive ended halfway, a propulsive vortex may not be formed and ejected. Any motion primitives that followed would thus need to re-pressurize the subumbrellar cavity.

Table 2. A summary of the geometry, physical, and flow characteristics for motion primitives of *A. victoria*.

Phase	Geometry/physical change	Flow effects
Bell compression	The bell compresses inward. The maximum thrust in the upstream direction is achieved. A local maximum for power is achieved.	There is strong outward flow across the velum. A hybrid relaxation-propulsive vortex is formed.
Vortex separation	The velar flap rotates inward. The bell continues to compress inward and the minimum exit diameter and cavity volume are achieved.	The hybrid relaxation-propulsive vortex separates from the hydromedusa.
Refill	The bell expands outward. The power output is highest due to the work performed during expansion. The drag is maximized initially and settles to a local minimum. A small upstream thrust is generated due to suction.	The inward flow rate increases rapidly due to a low pressure region drawing in fluid.
Vortex formation	The velar flap rotates outward. The suction effect subsides and the upstream thrust disappears.	Fluid continues to flow into the cavity. A relaxation vortex is also formed.
Coasting	The tip of the velar flap rotates outward slightly. An upstream thrust is generated.	The flow switches from inward to outward.

3.3. *Aequorea victoria* results and discussion

The observations of the *A. victoria*'s (L Murbach and C Shearer, 1902) movements were collected in the same manner as that for the *S. tubulosa*. Our experiments for *A. victoria* used a hydromedusa with a maximum and minimum bell radius of 2.3 cm and 1.9 cm, respectively. Additionally, the subumbrellar volume had a maximum value of approximately 10.5 cm^3 and a minimum value of 7.4 cm^3. Applying our generative model to a single, quasi-steady-state swimming cycle returned a total of five primitives, summaries of which are provided in table 2. The motion subsequences defined by these primitives are displayed in figures 6–10. For each subsequence, we have plotted the motion at four time steps. As before, we have superimposed the associated LCS.

Note that the selection of five primitives was automatically made by our model, not us. Although a swimming cycle of both *S. tubulosa* and *A. victoria* can be described with the same number of primitives, the motions and their effects are different.

3.3.1. Evaluating hydromedusa motions and their flow fields

From the plots in figure 6, it can be seen that the first primitive corresponds to a single motion taking place over 0.29 s. During this time, the majority of the velum is pulled inward. This bell contraction starts the vortex ejection by generating a shear layer on the bell interior. Ejecting this shear layer will result in a starting vortex with counter-clockwise rotation. There is also a relaxation vortex with clockwise vorticity present on the interior of the bell margin at the beginning of this primitive. The relaxation vortex was formed during the previous expansion phase and is clearly seen in the backward LCS. This relaxation vortex is ejected with the starting vortex during the contraction. These attracting material manifolds exhibit a strong similarity to results of previous dye visualization experiments by Dabiri *et al* [54] and Costello *et al* [55].

Not all of the fluid near the interior bell wall is expelled during contraction. The forward structures in figure 6 reveal that there is a pocket of fluid surrounded by a forward LCS that takes the place of the ejected fluid. The fluid within this forward LCS will eventually combine with the fluid outlined by the forward structure on the exterior of the hydromedusa to form the next relaxation vortex. While this vortex creation begins in the first primitive, it does not finish until the fifth.

The second primitive, as highlighted in figure 7, continues the propulsive rowing stage of the motion through the bell contraction and inward twisting of the velum. A byproduct of these two movements is the separation of the hybrid starting/relaxation vortex structure. During this primitive the fluid that made up the relaxation vortex begins to elongate due to the influence of the stronger starting vortex. Additionally, even though this vortex pair has been ejected, backward LCS remain that connect the ejected vortices to the tip of the bell. These backward structures represent an attracting material line of converging flow where dye or other particles will collect during swimming. There is negligible flow across these LCS.

When compared to the propulsive vortex of the *S. tubulosa*, there is a conspicuous lack of forward LCS for the vortex produced by *A. victoria*. This is due to the relatively small amount of stretching near the vortices in forward time due to the much weaker vortices generated by *A. victoria*. The slowly moving vortices of *A. victoria* move only about one body radius per swimming cycle compared to about 10 body radii per cycle for *S. tubulosa*, further indicating a much weaker vortex. Finally, the vortices generated by *A. victoria* are located away from the axis of symmetry. This is due to the paddling or rowing propulsion rather than the jetting propulsion used by *S. tubulosa*.

The third through fifth primitives, shown in figures 8–10, constitute the relaxation phase of the *A. victoria*, which lasts 0.64 s. During the third primitive, the bell of the hydromedusa begins to expand near the middle and drags the bell tip outwards while bending it slightly down. By the fourth primitive, the expansion has mostly ceased and only the outer fringes of the bell

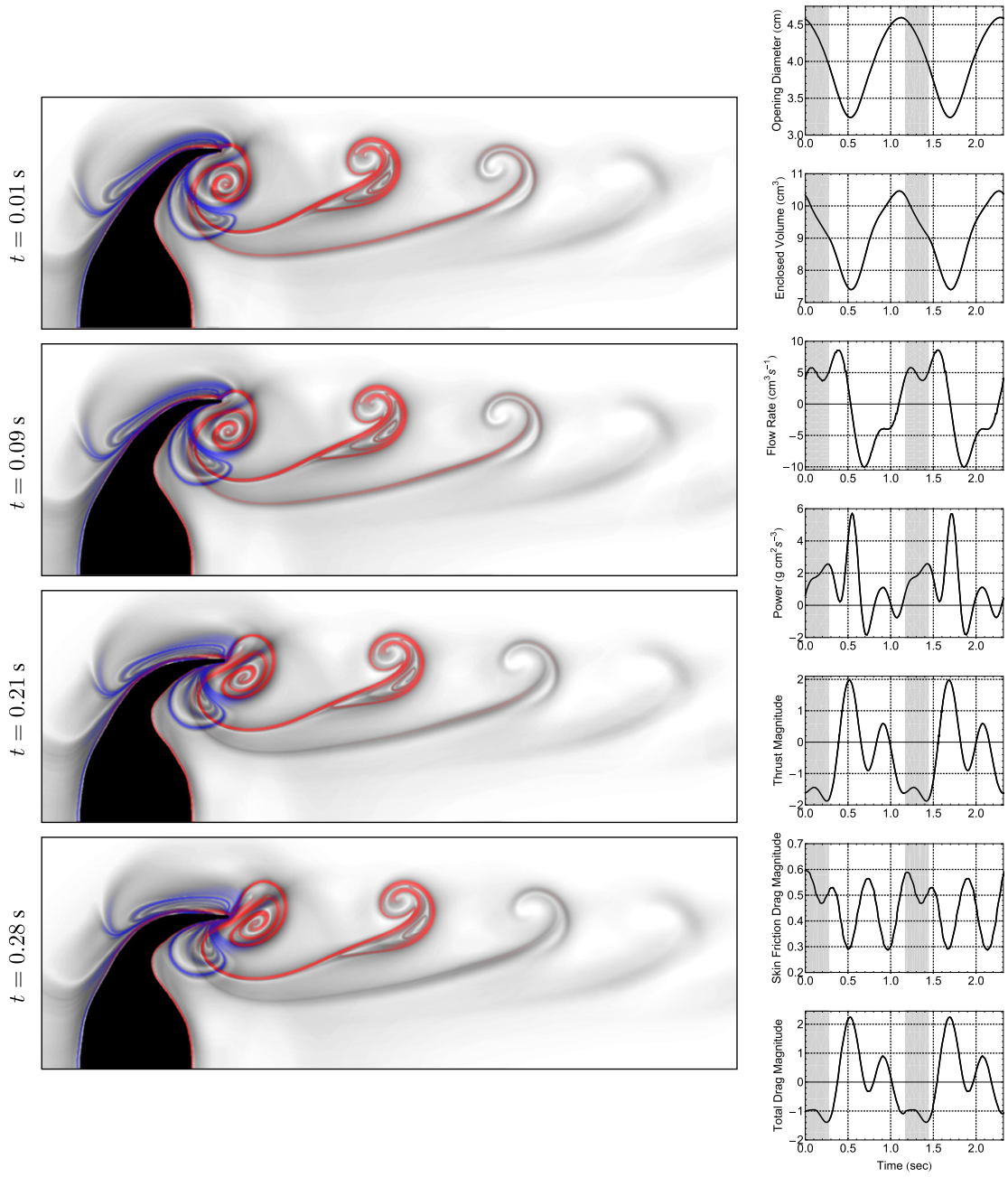

Figure 6. The first motion primitive, bell compression, for *A. victoria*, where the velar flap compresses and a propulsive-relaxation vortex is released. (left) Plots of the Lagrangian coherent structures for four near-equally spaced time steps over the duration of the primitive ($t = 0.01,\ 0.09,\ 0.21,\ 0.28$ s). Since the jellyfish is axisymmetric, we show only two-dimensional plots. In these plots, blue curves represent the forward structures and the red curves represent the backward structures. Mixtures of the forward and backward structures are given in gray, where the whiter values denote lower-magnitude transport. The bell of the hydromedusa is displayed in black. (right) Plots of the velar diameter, subumbrellar volume, flow rate, power output, thrust coefficient, total drag, and skin friction. In these plots, the gray shaded region denotes the time in which the motion primitive takes place. Since the propulsive motion was cyclic, we have plotted two periods.

flex outward. There are few movements that occur for the final primitive, and those that do serve to only slightly shift the velar tip.

3.3.2. *Evaluating hydromedusa motions and dynamics quantities*

The motion primitives shown in figures 6–10 show promise for use as controllers. This is because the distinct modes present in each motion primitive represent discrete body motions associated with muscular actuations. Such changes in muscular forcing may be decomposed for further optimization for a desired purpose.

To substantiate that there are unique dynamics and forces for each primitive, we have plotted various physical quantities in figures 6–10. The quantity that we contemplate are the velar opening diameter and subumbrellar volume. From a cursory inspection, it can be seen that the breakpoints closely track trends in these two measurements. During the course of the bell

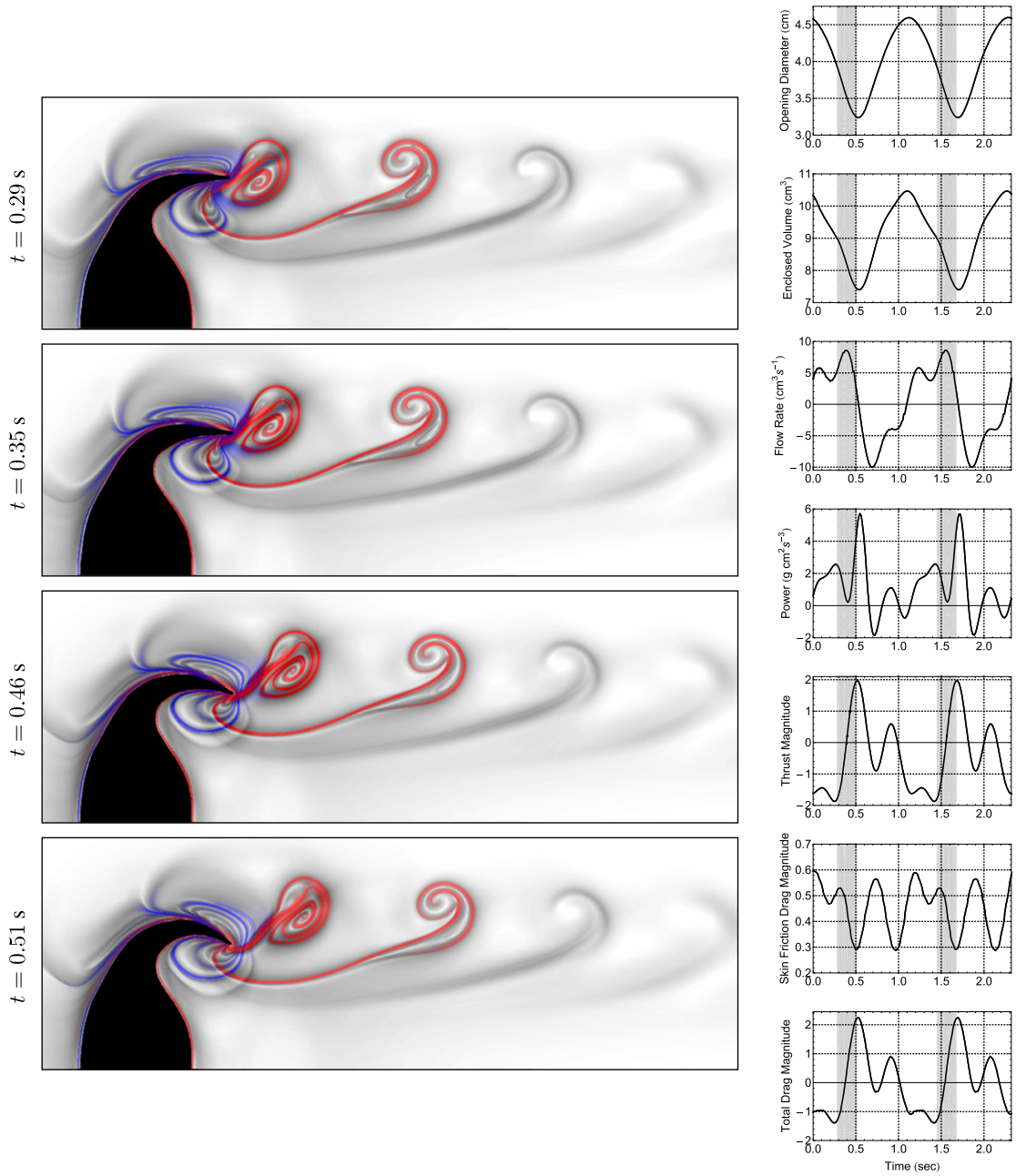

Figure 7. The second motion primitive, vortex separation, for *A. victoria*, where the velar flap curls inward and pinches off the vortex. (left) Plots of the Lagrangian coherent structures for four near-equally spaced time steps over the duration of the primitive ($t = 0.29,\ 0.35,\ 0.46,\ 0.51$ s). Since the jellyfish is axisymmetric, we show only two-dimensional plots. In these plots, blue curves represent the forward structures and the red curves represent the backward structures. Mixtures of the forward and backward structures are given in gray, where the whiter values denote lower-magnitude transport. The bell of the hydromedusa is displayed in black. (right) Plots of the velar diameter, subumbrellar volume, flow rate, power output, thrust coefficient, total drag, and skin friction. In these plots, the gray shaded region denotes the time in which the motion primitive takes place. Since the propulsive motion was cyclic, we have plotted two periods.

compression and vortex separation primitives, both values monotonically decrease as the vortex ring is released. Similarly, over a majority of the last three primitives, the values constantly increase as the subumbrellar cavity is refilled. We surmise that the breakpoints for *A. victoria* were better correlated with dynamics than those for *S. tubulosa* due to the nature of the propulsive mechanisms. More specifically, the inertial forces generated by paddling are sensitive to the bell characteristics, since they can either peak or drop at the stroke transitions [56].

As we briefly touched on above, the low formation time signals a thin cored vortex ring, whereby the maximum axial velocity is moved outward radially from the central axis. The same conclusion can be reached from inspection of the coherent structures. That is, the velocity dominates near the bell margins and quickly decays as the radial distance beyond the

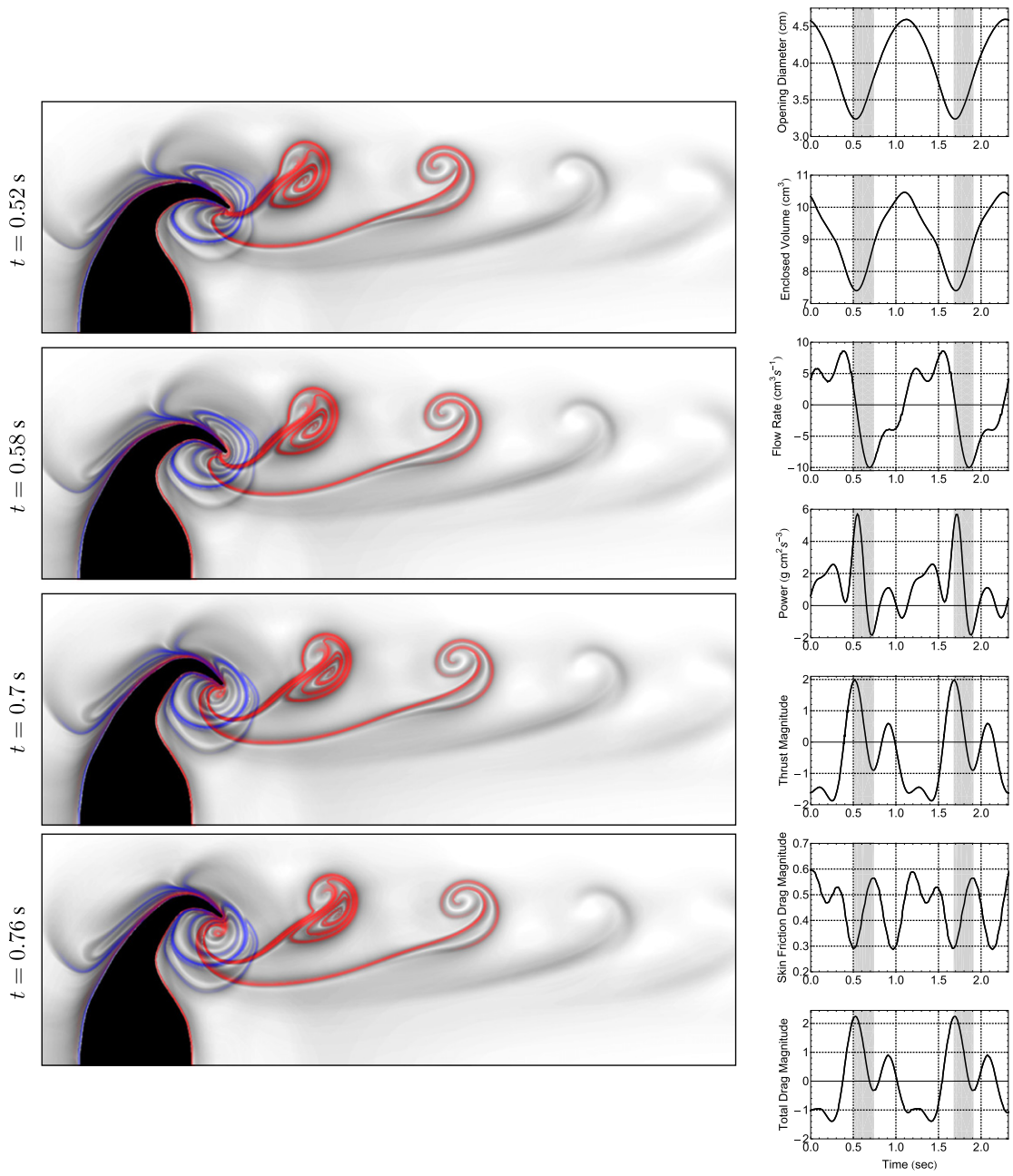

Figure 8. The third motion primitive, refill, for *A. victoria*, where the bell expands near the middle and pulls in fluid. (left) Plots of the Lagrangian coherent structures for four near-equally spaced time steps over the duration of the primitive ($t = 0.52,\ 0.58,\ 0.7,\ 0.76$ s). Since the jellyfish is axisymmetric, we show only two-dimensional plots. In these plots, blue curves represent the forward structures and the red curves represent the backward structures. Mixtures of the forward and backward structures are given in gray, where the whiter values denote lower-magnitude transport. The bell of the hydromedusa is displayed in black. (right) Plots of the velar diameter, subumbrellar volume, flow rate, power output, thrust coefficient, total drag, and skin friction. In these plots, the gray shaded region denotes the time in which the motion primitive takes place. Since the propulsive motion was cyclic, we have plotted two periods.

boundary grows, leaving the flow largely undisturbed. These results greatly differ from those of *S. tubulosa*, which produced velocity disturbances only near the axis of symmetry. Additionally, the coasting phase for *A. victoria* is shorter, and each swimming cycle is essentially a continuous transition from contraction to relaxation and back to contraction. Due to these distinctions, it is not possible to calculate the average pressure and power output for *A. victoria* in the simple fashion we did for *S. tubulosa*.

Since the cavity is only weakly pressurized, we approximate the work done via an alternate representation: as a normalized, temporal integral of the power output from the surface of the hydromedusa to the surrounding fluid [2]. The associated plots for this term reveal that the motion segmentation closely conforms with its evolution. Throughout the bell compression primitive, the power coefficient steadily grows, due to the vorticity flux, and reaches a local maximum value. During the vortex separation

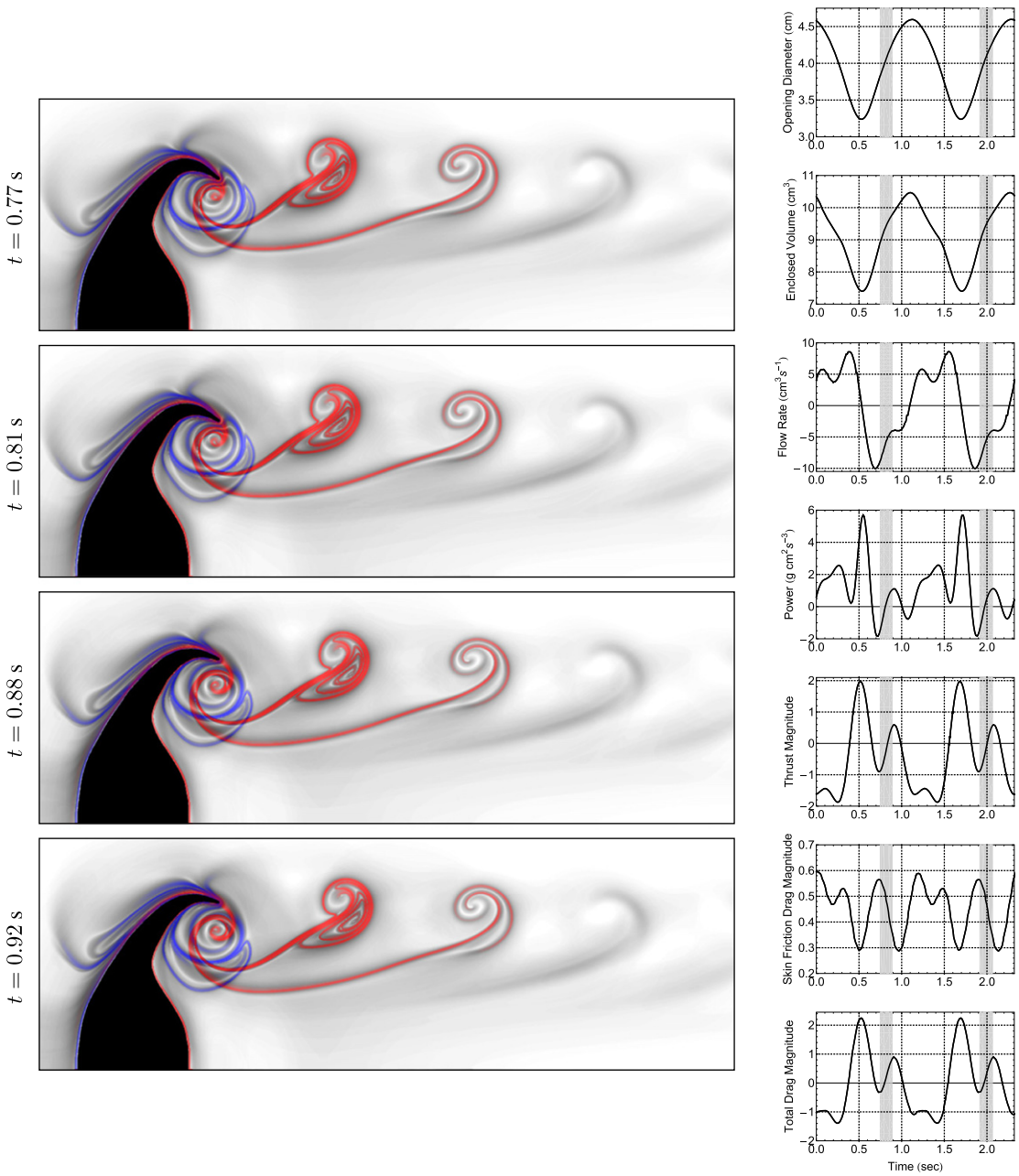

Figure 9. The fourth motion primitive, vortex formation, for *A. victoria*, where the tip of the velum curls outward and a relaxation vortex develops. (left) Plots of the Lagrangian coherent structures for four near-equally spaced time steps over the duration of the primitive ($t = 0.77,\ 0.81,\ 0.88,\ 0.92$ s). Since the jellyfish is axisymmetric, we show only two-dimensional plots. In these plots, blue curves represent the forward structures and the red curves represent the backward structures. Mixtures of the forward and backward structures are given in gray, where the whiter values denote lower-magnitude transport. The bell of the hydromedusa is displayed in black. (right) Plots of the velar diameter, subumbrellar volume, flow rate, power output, thrust coefficient, total drag, and skin friction. In these plots, the gray shaded region denotes the time in which the motion primitive takes place. Since the propulsive motion was cyclic, we have plotted two periods.

primitive, the power quickly drops then raises. The former event is likely due to a modest influx of fluid into the subumbrellar cavity around the oral opening, which is confirmed by the dip in the flow rate, thrust, and total drag. The refill primitive sees a huge increase in power output. At the beginning of the primitive there is a large acceleration in cavity volume and the half-sink-like acceleration circulation results in a simultaneous peak in thrust. Unlike *S. tubulosa*, the peak in thrust and power for *A. victoria* could hypothetically result in lower relative power since the boundary velocity moving against these pressure forces is low [43]. At the end of the refill primitive the acceleration terms become negligible and the power becomes negative, signifying that the fluid is doing work on the jellyfish. During the vortex formation and coasting primitives, there are fluctuations in the power. These fluctuations likely stem from the flexing of the velar flap. That is, the flap moves in a way that causes the low-pressure

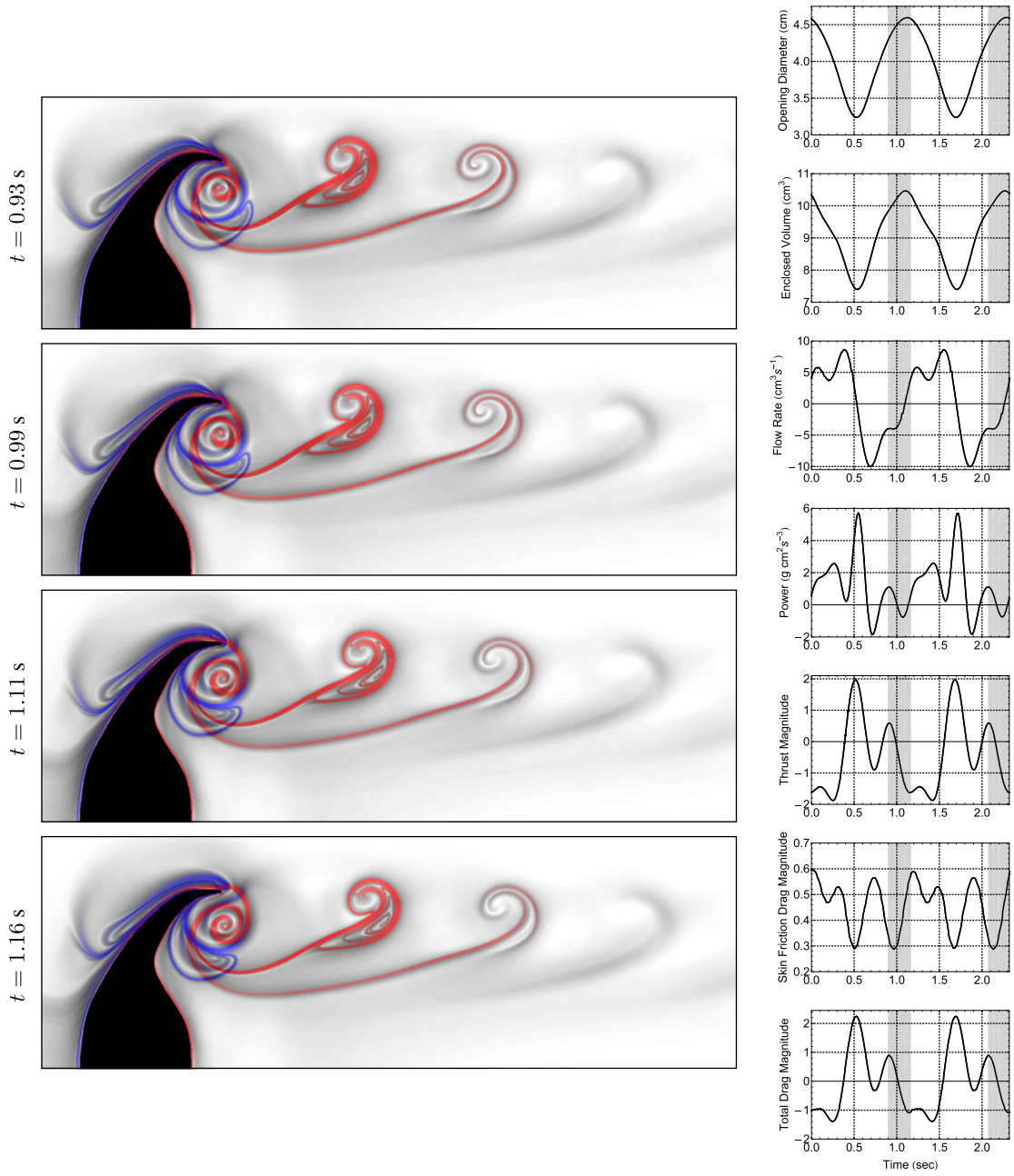

Figure 10. The fifth motion primitive for *A. victoria*, which is a coasting phase. (left) Plots of the Lagrangian coherent structures for four near-equally spaced timesteps over the duration of the primitive ($t = 0.93,\ 0.99,\ 1.11,\ 1.16$ s). Since the jellyfish is axisymmetric, we show only two-dimensional plots. In these plots, blue curves represent the forward structures and the red curves represent the backward structures. Mixtures of the forward and backward structures are given in gray, where the whiter values denote lower-magnitude transport. The bell of the hydromedusa is displayed in black. (right) Plots of the velar diameter, subumbrellar volume, flow rate, power output, thrust coefficient, total drag, and skin friction. In these plots, the gray shaded region denotes the time in which the motion primitive takes place. Since the propulsive motion was cyclic, we have plotted two periods.

relaxation vortex to create a suction effect, which yields thrust in the upstream direction [57, 58].

From this analysis, we may infer that the conventional division of motion into either contraction or expansion is a bit coarse. There is, in fact, a more diverse aggregation of movements, which becomes obvious once paired with the dynamics. Akin to the breakpoints for the *S. tubuolsa*, those for *A. victoria* begin when there is no variation in force and when there is a switch in movement direction and speed for some portion of the anatomy. This leads us to again believe that such primitives have some utility for path planning and control.

We feel it prudent to mention that, from a control standpoint, it is advantageous to have a large number of short-term primitives versus fewer longer-term ones. The former case provides an opportunity to interrupt a planned course and handle unforeseen events. Comparably, the latter could pose problems in certain scenarios. One instance that we can envision entails the dissipation of the relaxation vortex, either

from a large shear gradient in the flow or the passage of enough time without meaningful motion. The loss of this vortex would adversely affect propulsion efficiency for oblate-based platforms, as the kinetic energy lost in the wake would be increased due to a higher fluid rotation [54].

The *S. tubuolsa* takes advantage of its jetting cycle to produce large accelerations that help it escape predators and reposition itself for feeding. In contrast, the *A. victoria* experiences much lower accelerations and uses swimming as an extension of its feeding mechanism. Aside from the physical differences, the negative velocities along the symmetry axis indicate that a large, added mass force hinders its actions. Although *A. victoria* has a lower overall thrust, metrics like the Froude coefficient show it to be more efficient. While it might be tempting to think that nature has perfected the motions, we hypothesize that there are ample opportunities to further enhance them for specific applications. For example, a higher stroke amplitude during *A. victoria*'s fourth and fifth primitives should, over the first and second primitives, export a larger net energy into the wake as a strong vortex shedding. Such an alteration will promote faster swimming, albeit at the expensive of a higher locomotive cost. As another instance, if we increased the pulsing frequency, we would expect a higher circulation shedding rate and hence a higher overall velocity. However, the effort required to achieve this would likely be more than if we simply adjusted the stroke amplitude [59].

4. Conclusions

We have developed a systematic approach for segmenting and characterizing the non-rigid-body motions of hydromedusae. The essence of our approach is twofold. The first component is a hierarchical, Bayesian statistical model that relies on latent stochastic processes to mathematically describe the body deformations. The latent processes act as high-dimensional dynamical systems over parts of the phase space. The other component is a projection-based mixture model for constructing coarse-grained versions of the models on a reduced space. Due to the judicious selection of nonparametric priors, the model can adapt to the observed hydromedusae motions and self-tune its parameters. This functionality is particularly helpful: it permits the number of motion subsequences, or motion primitives, to be determined automatically in an unsupervised manner.

Through experiments with the jetting-based *S. tubulosa* and rowing-based *A. victoria*, our model identified five motion primitives for each species. In the case of *S. tubulosa*, the first motion primitive corresponds to the pressurization of the subumbrellar cavity in preparation for the creation of a propulsive jet. This is followed by jet formation and jetting primitives. Most of the work performed by the hydromedusa takes place during these latter two primitives. The fourth primitive encompasses a refill phase and serves to draw in surrounding fluid for the next swimming cycle. The movement of fluid around the subumbrellar flap and into the cavity leads to the formation of a relaxation vortex. The remaining motion primitive is a passive coasting stage, whereby the hydromedusa relies on momentum delivered into the wake to move upstream. For each of these primitives, we have established links between the temporal breakpoints and transitions in dynamics trends. This finding validates that our breakpoints are not occurring at random instants and hence have physical significance. It also alludes that a great deal of dynamics information is already present in the movements and that they are a promising modality for analysis.

The motion primitives for *A. victoria* are distinct from those of *S. tubulosa*, which stems from morphological differences. During the first primitive for *A. victoria*, a hybrid propulsive-relaxation vortex is formed by a compression of the bell. This vortex separates in the second primitive. Due to the release of elastic strain energy, the bell begins to expand outward in the third primitive. This expansion triggers the creation of a low-pressure region inside the cavity, which pulls in surrounding fluid. The fourth primitive corresponds with the formation of a relaxation vortex. A brief coasting phase is observed in the fifth primitive. As with the motion primitive breakpoints for *S. tubulosa*, those for *A. victoria* occur during meaningful changes in both body kinematics and flow field patterns. We therefore believe that the identified motion primitives encode unique actuation regimes.

The approach developed in this paper represents part of the foundation for automating biomimetic control. In our future endeavors, we will be using this approach to analyze a wide range of swimming maneuvers and characterize them as stochastic dynamical systems. We envision eventually stringing together series of these dynamical-systems-based motion primitives to control a soft-robotics platform. As well, we intend to exploit properties of the motion primitives to motivate the placement of actuators in such platforms and determine a good number of such actuators.

Appendix. Nonparametric Bayesian inference

To apply the model in (4) to segment motions, we will need to ascertain the posterior distribution of the unknown parameters. Like most non-trivial Bayesian models, the distribution is not directly calculable. We thus turn to approximate inference and, in particular, to Markov chain Monte Carlo samplers [41]. Such samplers are principled random walks that simulate an aperiodic, irreducible Markov chain with the posterior as the invariant distribution.

The generative story outlined above is rather complicated, so we have elected to break it apart and tackle the Gauss–Markov section separately. Before we can deal with this section, though, there is one issue with the current model: it is infinite twice over, as there are an infinite number of Poisson processes which each contain an infinite number of points. To circumvent this issue, we first pare the number of points to a finite amount such that $\tau_{i,k}^m$ is restricted to a region defined by $a_{k;\tau}^m$ and $b_{k;\tau}^m$, which leads to

$$\kappa_k^m(t)^2 \approx \sum_{j=1}^{\infty}\sum_{i=1}^{n_j} e^{t\tau_{i,k}^m - t\lambda_{i,k}^m}\vartheta_{i,j,k}^m \delta_{\tau_{i,k}^m < t}.$$

Next, we seek a finite set of processes that contain all Poisson processes with one or more points in that region,

$$\kappa_k^m(t)^2 \approx \sum_{j=1}^{n_d}\sum_{i=1}^{n_j} e^{t\tau_{i,k}^m - t\lambda_{i,k}^m}\vartheta_{i,j,k}^m \delta_{\tau_{i,k}^m < t},$$

where $\sum_{j=d+1}^{\infty} n_j = 0$ and $n_d > 0$.

The jump sizes $\vartheta_{i,j}^m$ for the marked Poisson process can be altered, one by one, according to a Metropolis–Hastings rule [60, 61], where a new value $\log \vartheta_{i,j}'^m \sim \log \vartheta_{i,j}^m + \epsilon$, $\epsilon \sim \text{Normal}(a_\vartheta, b_\vartheta^2)$, is accepted in agreement with the proposal

$$\text{pr}\left(y_{l,k}^m(t)\middle|\vartheta_{i,j}'^m \cdots\right)\vartheta_{i,j}'^m q_\vartheta\left(\vartheta_{i,j}'^m\right)2^\vartheta \times \sum_{r=1}^{2^\vartheta}\psi_r^m \delta_{\vartheta_{i,j}'^m \in \mathcal{Q}_\vartheta^{-1}\left((r-1)/2^\vartheta\right),\mathcal{Q}_\vartheta^{-1}\left(r/2^\vartheta\right)}.$$

The corresponding jump times $\tau_{i,j}^m$ have a simple update and is skipped here. As for the trim sizes of the Poisson process, we look to a reversible-jump sampler [62].

The intensities of the Poisson process are emended separately. That is, if $n_j = 0$, $w_{j,l,k}'^m = w_{j,l,k}^m + \epsilon_w$, $\epsilon_w \sim \text{Normal}(a_w, b_w^2)$ and we let $w_{j,l,k}''^m$ be the smallest value of $w_{1,l,k}^m, \ldots, w_{j,l,k}^m, \ldots$ and $w_{l,k}'''^m$ be the smallest value of $w_{1,l,k}^m, \ldots, w_{j,l,k}''^m, \ldots$, the move is approved according to

$$\begin{aligned}&\text{pr}\left(y_{l,k}^m(t)\middle|w_{j,l,k}'^m \cdots\right)\\ &\times \exp\left(w_{l,k}'^m - w_{l,k}^m\right)\exp\left(1+\psi_{l,k}^m\left(a_{k;\tau}^m - b_{k;\tau}^m\right)\right)\\ &\times \exp\left(\varphi_k^m\int_{w_k''^m}^{w_k'''^m}\left(1-\left(a_{k;\tau}^m - b_{k;\tau}^m\right)\right)e^\mu/\mu d\mu\right.\\ &\left.+\ \varphi_k^m\int_{w_k'''^m}^{\infty} e^\mu/\mu d\mu - \varphi_k^m\int_{w_k''^m}^{\infty} e^\mu/\mu d\mu\right)\end{aligned}$$

if $w_{l,k}'''^m > w_{j,l,k}''^m$. If $w_{l,k}'''^m < w_{j,l,k}''^m$, then the approval is almost the same, as only the limits for the left-most integral are swapped. On the other hand, if $n_j = 0$, $w_{j,l,k}'^m \sim \text{Gamma}(n_j,\ 1+\psi_{l,k}^m(a_{\rho,k}^m - b_{\rho,k}^m))$, which is admitted by

$$\begin{aligned}&\text{pr}\left(y_{l,k}^m(t)\middle|w_{j,l,k}'^m \cdots\right)\\ &\times (\varphi_k^m\int_{w_k''^m}^{w_k'''^m}\left(1-\left(a_{k;\tau}^m - b_{k;\tau}^m\right)\right)e^\mu/\mu d\mu\\ &+\ \varphi_k^m\int_{w_k'''^m}^{\infty} e^\mu/\mu d\mu - \varphi_k^m\int_{w_k''^m}^{\infty} e^\mu/\mu d\mu\Big)\end{aligned}$$

if $w_{l,k}'''^m > w_{j,l,k}''^m$; if $w_{l,k}'''^m < w_{j,l,k}''^m$; the upper and lower limits of the left-most integral are again switched.

Note that the rate at which Metropolis–Hastings steps are taken can affect the search undertaken by the Markov chain. To avoid slow convergence, we implement a multiple-try variant [63].

An advantage of the Bayesian formalism is that the inferred posterior density may be employed to make probabilistic predictions about the relevancy of the model at future time instants and appraise the model's goodness-of-fit [64]. Both capabilities can be realized through Monte Carlo integration alongside the main inference procedure. The reason that this is possible is that the Bayesian formalism provides a non-arbitrary, non-heuristic way to determine how skeptical one should be of the model outcomes. Such functionality is decisive whenever an initial subset of data provides a tenuous account of the system behavior. It is also useful for rejecting low-performing models. Lastly, this functionality allows the model to communicate when additional data should be used to enhance the model performance.

If additional observations would help improve the model's quality, it would be convenient to incorporate them without having to abandon the current model. Toward this end, we look to particle filters [42].

Acknowledgments

The work of the authors was funded by the US Office of Naval Research. The work of the first author was additionally funded by a University of Florida Graduate Fellowship and a Robert C Pittman Research Fellowship.

References

[1] Krieg M and Mohseni K 2012 New perspective on collagen fibers in the squid mantle *J. Morphol.* **273** 586–95
[2] Sahin M, Mohseni K and Colin S P 2009 The numerical comparison of flow patterns and propulsive performances for the hydromedusae *Sarsia tubulosa* and *Aequorea victoria J. Exp. Biol.* **212** 2656–67
[3] Leonard J L 1980 Temporal organization of swimming activity in *Sarsia tubulosa* M. Sars (hydrozoa) *J. Comparative Physiol.* **136** 219–25
[4] Mills C E 1981 Diversity of swimming behavior in hydromedusae as related to feeding and utilization of space *Mar. Biol.* **64** 185–9
[5] Gladfelter W B 1972 Structure and function of the locomotory system of Polyorchis montereyensis (cnidaria, hydrozoa) *Helgoländer Wiss. Meeresuntersuchungen* **23** 38–79
[6] Donaldson S, Mackie G O and Roberts A 1980 Preliminary observations on escape swimming and giant neurons in

Aglantha digitale (hydromedusae: trachylina) *Can. J. Zool.* **58** 549–52
[7] Daniel T L 1983 Mechanics and energetics of medusan jet propulsion *Can. J. Zool.* **61** 1406–20
[8] Daniel T L 1985 Cost of locomotion: unsteady medusan swimming *J. Exp. Biol.* **119** 149–64
[9] Colin S P and Costello J H 2002 Morphology, swimming performance and propulsive mode of six co-occurring hydromedusae *J. Exp. Biol.* **205** 427–37
[10] Lipinski D and Mohseni K 2009 Flow structures and fluid transport for the hydromedusae *Sarsia tubulosa* and *Aequorea victoria J. Exp. Biol.* **212** 2436–47
[11] McHenry M J and Jed J 2003 The ontogenetic scaling of hydrodynamics and swimming performance in jellyfish a Aurelia auritaa *J. Exp. Biol.* **206** 4125–37
[12] Satterlie R A and Spencer A N 1983 Neuronal control of locomotion in hydrozoan medusae *J. Comparative Physiol.* **150** 195–206
[13] Satterlie R A 2002 Neuronal control of locomotion in hydrozoan medusae: a comparative story *Can. J. Zool.* **80** 1654–69
[14] Nawroth J C, Lee H, Feinberg A W, Ripplinger C M, McCain M L, Grosberg A, Dabiri J O and Parker K K 2012 A tissue-engineered jellyfish with biomimetic propulsion *Nat. Biotechnol.* **30** 792–7
[15] Krieg M and Mohseni K 2008 Thrust characterization of a bioinspired vortex ring thruster for locomotion of underwater robots *IEEE J. Ocean. Eng.* **33** 123–32
[16] Krieg M and Mohseni K 2010 Dynamic modeling and control of biologically inspired vortex ring thrusters for underwater robot locomotion *IEEE Trans. Robot.* **26** 542–54
[17] Dudek G and Simhon S 2003 Path planning using learned constraints and preferences *Proc. IEEE Int. Conf. Robotics and Automation* (*ICRA*) (*Taipei, Taiwan, 14–19 September 2003*) pp 2907–2913
[18] Jäkel R, Schmidt-Rohr S R, Lösch M and Dillmann R 2010 Representation and constrained planning of manipulation strategies in the context of programming by demonstration *Proc. IEEE Int. Conf. Robotics and Automation aICRAa* (*Anchorage, AK, 3–7 May 2010*) pp 162–169
[19] Cohen B J, Chitta S and Likhachev M 2010 Search-based planning for manipulation with motion primitives *Proc. IEEE Int. Conf. Robotics and Automation* (*ICRA*) (*Anchorage, AK, 3–7 May 2010*) pp 2902–2908
[20] Cohen B J, Subramanian G, Chitta S and Likhachev M 2011 Planning for manipulation with adaptive motion primitives *Proc. IEEE Int. Conf. Robotics and Automation* (*ICRA*) (*Shanghai, China, 9–13 May 2011*) pp 5478–5485
[21] Powell M J, Zhao H and Ames A D 2012 Motion primitives for human-inspired bipedal robotic locomotion: walking and stair climbing *Proc. IEEE Int. Conf. Robotics and Automation* (*ICRA*) (*saint Paul MN, 14–18 May 2012*) pp 543–9
[22] Lee D and Nakamura Y 2006 Stochastic model of imitating a new observed motion based on the aquired motion primitives *Proc. IEEE/RSJ Int. Conf. Intelligent Robots and Systems* (*IROS*) (*Beijing, China, 9–15 October 2006*) pp 4994–5000
[23] Lee D and Ott C 2010 Incremental motion primitive learning by physical coaching using impedence control *Proc. IEEE/RSJ Int. Conf. Intelligent Robots and Systems* (*IROS*) (*Taipei, Taiwan, 18–22 October 2010*) pp 4133–4140
[24] Kulić D, Takano W and Nakamura Y 2008 Incremental learning, clustering and hierarchy formation of whole body motion patterns using adaptive hidden Markov chains *Int. J. Robot. Res.* **27** 761–84
[25] Kulić D, Ott C, Lee D, Ishikawa J and Nakamura Y 2011 Incremental learning of full body motion primitives and their sequencing through human motion observation *Int. J. Robot. Res.* **31** 330–45
[26] Bertoin J 1996 *Lévy Processes* (Cambridge: Cambridge University Press)
[27] Sato K-I 1999 *Lévy Processes and Infinitely Divisible Distributions* (Cambridge: Cambridge University Press)
[28] Berman S M 1994 A bivariate Markov process with diffusion and discrete components, communications in statistics *Stoch. Models* **20** 271–308
[29] Schach S 1971 Weak convergence results for a class of multivariate Markov processes *Ann. Math. Stat.* **42** 451–65
[30] McNeil D R and Schach S 1973 Central limit analogues for Markov population processes *J. R. Stat. Soc.* B **35** 1–23
[31] Diggle P J 1988 An approach to the analysis of repeated measurements *Biometrics* **44** 959–71
[32] Müller P and Quintana F A 2004 Nonparametric Baysian data analysis *Stat. Sci.* **19** 95–110
[33] Oksendal B 2010 *Stochastic Differential Equations* (New York: Springer)
[34] Doob J L 1942 The Brownian movement and stochastic equations *Ann. Math.* **43** 351–69
[35] Liechty J C and Roberts G O 2001 Markov chain Monte Carlo methods for switching diffusion models *Biometrika* **88** 299–315
[36] Bishop C M and Lasserre J 2007 Generative or discriminative? Getting the best of both worlds *Bayesian Statistics 8* ed J M Bernardo *et al* (Oxford: Oxford University Press) pp 3–23
[37] Ferguson T S and Klass M J 1972 A representation of independent increment processes without Gaussian components *Ann. Math. Stat.* **43** 1634–43
[38] Cox D R and Isham V I 1980 *Point Processes* (London: Chapman and Hall)
[39] Ferguson T S 1974 Prior distributions on spaces of probability measures *Ann. Stat.* **2** 615–29
[40] Lavine M 1992 Some aspects of Pólya tree distributions for statistical modeling *Ann. Stat.* **20** 1222–35
[41] Robert C and Casella G 2004 *Monte Carlo Statistical Methods* (New York: Springer)
[42] Doucet A and de Freitas N 2001 *Sequential Monte Carlo Methods in Practice* ed N Gordon (New York: Springer)
[43] Krieg M and Mohseni K 2015 Pressure and work analysis of unsteady, deformable, axisymmetric, jet producing cavity-bodies *J. Fluid Mech.* **769** 337–68
[44] Krieg M and Mohseni K 2013 Modelling circulation, impulse and kinetic energy of starting jets with non-zero radial velocity *J. Fluid Mech.* **719** 488–526
[45] Haller G and Yuan G 2000 Lagrangian coherent structures and mixing in two-dimensional turbulence *Physica* D **147** 352–70
[46] Shadden S C, Lekien F and Marsden J E 2005 Definition and properties of lagrangian coherent structures from finite-time lyapunov exponents in two-dimensional aperiodic flows *Physica* D **212** 271–304
[47] Sahin M and Mohseni K 2009 An arbitrary Lagrangian–Eulerian formulation for the numerical simulation of flow patterns generated by the hydromedusa aequorea victoria *J. Comput. Phys.* **228** 4588–605
[48] Hirt C W, Amsden A A and Cook J L 1974 An arbitrary Lagrangian–Eulerian computing method for all flow speeds *J. Comput. Phys.* **14** 277–253
[49] Sahin M 2005 A preconditioned semi-staggered dilation-free finite volume method for the incompressible navier-stokes equations on all-hexahedral elements *Int. J. Numer. Methods Fluids* **49** 959–74
[50] Saad Y and Schultz M H 1986 GMRES: a generalized minimal residual algorithm for solving nonsymmetric linear systems *SIAM J. Sci. Stat. Comput.* **7** 856–69
[51] Johnson A A and Tezduyar T E 1994 Mesh update strategies in parallel finite element computations of flow problems with moving boundaries and interfaces *Comput. Methods Appl. Mech. Eng.* **119** 73–94
[52] Satterlie R A 2011 Do jellyfish have central nervous systems? *J. Exp. Biol.* **214** 1215–23
[53] Dabiri J O, Colin S P and Costello J H 2006 Fast-swimming hydromedusae exploit velar kinematics to form an optimal vortex wake *J. Exp. Biol.* **209** 2025–33

[54] Dabiri J O, Colin S P and Costello J H 2007 Morphological diversity of medusan lineages constrained by animal-fluid interactions *J. Exp. Biol.* **210** 1868–73
[55] Costello J H, Colin S P and Dabiri J O 2008 Medusan morphospace: Phylogenetic constraints, biomechanical solutions, and ecological consequences *Invertebrate Biol.* **127** 265–90
[56] Vogel S 1994 *Life in Moving Fluids* (Princeton, NJ: Princeton University Press)
[57] Sahin M, Mohseni K and Colin S P 2009 The numerical comparison of flow patterns and propulsive performances for the hydromedusae *Sarsia tubulosa* and *Aequorea victoria J. Exp. Biol.* **212** 2656–67
[58] Sahin M and Mohseni K 2009 An arbitrary Lagrangian–Eulerian formulation for the numerical simulation of flow patterns generated by the hydromedusa Aequorea victoria *J. Comput. Phys.* **228** 4588–605
[59] Peng J and Alben S 2012 Effects of shape and stroke parameters on the propulsion performance of an axisymmetric swimmer *Bioinspiration Biomimetics* **7** 016012
[60] Hastings W K 1969 Monte carlo sampling methods using Markov chains and their applications *Biometrika* **57** 97–109
[61] Peskun P H 1973 Optimum Monte-Carlo sampling using markov chains *Biometrika* **60** 607–12
[62] Green P J 1995 Reversible jump Markov chain Monte Carlo computation and Bayesian model determination *Biometrika* **82** 711–32
[63] Liu J S, Liang F and Wong W H 2000 The multiple-try method and local optimization in metropolis sampling *J. Am. Stat. Assoc.* **95** 121–34
[64] Gelman A, Meng X-L and Stern H 1996 Posterior predictive assessment of model fitness via realized discrepancies *Stat. Sinica* **6** 733–808